Genetic requirement of *dact1/2* to regulate noncanonical Wnt signaling and *calpain 8* during embryonic convergent extension and craniofacial morphogenesis

Shannon H. Carroll[1,2,3,], Sogand Schafer[1,2], Kenta Kawasaki[2,3], Casey Tsimbal[2,3], Amélie M. Julé[4], Shawn A. Hallett[2,3], Edward Li[2] and Eric C. Liao[1,2,3]

[1]Center for Craniofacial Innovation, Children's Hospital of Philadelphia Research Institute, Children's Hospital of Philadelphia, PA 19104, USA.

[2]Division of Plastic and Reconstructive Surgery, Department of Surgery, Children's Hospital of Philadelphia, PA 19104, USA.

[3]Shriners Hospital for Children, Tampa, FL 33607, USA

[4] Department of Biostatistics, Harvard T.H. Chan School of Public Health, Boston, MA 02115, USA

Abstract

Wnt signaling plays crucial roles in embryonic patterning including the regulation of convergent extension during gastrulation, the establishment of the dorsal axis, and later, craniofacial morphogenesis. Further, Wnt signaling is a crucial regulator of craniofacial morphogenesis. The adapter proteins Dact1 and Dact2 modulate the Wnt signaling pathway through binding to Disheveled. However, the distinct relative functions of Dact1 and Dact2 during embryogenesis remain unclear. We found that *dact1* and *dact2* genes have dynamic spatiotemporal expression domains that are reciprocal to one another suggesting distinct functions during zebrafish embryogenesis. Both *dact1* and *dact2* contribute to axis extension, with compound mutants exhibiting a similar convergent extension defect and craniofacial phenotype to the *wnt11f2* mutant. Utilizing single-cell RNAseq and an established noncanonical Wnt pathway mutant with a shortened axis (*gpc4*), we identified *dact1/2* specific roles during early development. Comparative whole transcriptome analysis between wildtype and *gpc4* and wildtype and *dact1/2* compound mutants revealed a novel role for *dact1/2* in regulating the mRNA expression of the classical calpain *capn8*. Over-expression of *capn8* phenocopies *dact1/2* craniofacial dysmorphology. These results identify a previously unappreciated role of *capn8* and calcium-dependent proteolysis during embryogenesis. Taken together, our findings highlight the distinct and overlapping roles of *dact1* and *dact2* in embryonic craniofacial development, providing new insights into the multifaceted regulation of Wnt signaling.

Introduction

Wnt signaling is a crucial regulator of embryogenesis through its regulation of body axis patterning, cell fate determination, cell migration, and cell proliferation (Logan and Nusse 2004, Steinhart and Angers 2018, Mehta, Hingole et al. 2021). Current mechanistic understanding of Wnt signaling during embryogenesis includes an extensive catalog of ligands, receptors, co-receptors, adaptors, and effector molecules (Clevers and Nusse 2012, Niehrs 2012, Loh, van Amerongen et al. 2016, Mehta, Hingole et al. 2021). The intricate spatiotemporal integration of Wnt signaling combinations is an important focus of developmental biology and tissue morphogenesis (Petersen and Reddien 2009, Clevers and Nusse 2012, Loh, van Amerongen et al. 2016, Wiese, Nusse et al. 2018). Disruptions of Wnt signaling-associated genes lead to several congenital malformations which often affect multiple organ systems given their pleotropic developmental functions (Hashimoto, Morita et al. 2014, Shi 2022). Craniofacial anomalies are among the most common structural congenital malformations and genes in the Wnt signaling pathway are frequently implicated (Ji, Hao et al. 2019, Reynolds, Kumari et al. 2019, Huybrechts, Mortier et al. 2020).

Genetic approaches in zebrafish have identified a number of key Wnt regulators of early development, with gastrulation and craniofacial phenotypes (Brand, Heisenberg et al. 1996, Hammerschmidt, Pelegri et al. 1996, Heisenberg, Brand et al. 1996, Piotrowski, Schilling et al. 1996, Solnica-Krezel, Stemple et al. 1996, Schilling and Le Pabic 2009). The *silberblick (slb)* mutant, later identified as a *wnt11f2* mutant allele, exhibits gastrulation and midline craniofacial phenotypes that encompassed aspects of multiple

63 mutant classes. During early segmentation in the somite stage, the *wnt11f2* mutant
64 developed a shortened anterior-posterior axis and partially fused eyes (Heisenberg,
65 Brand et al. 1996). Subsequently, as the cranial prominences converge and the ethmoid
66 plate (EP) formed, instead of a fan-shaped structure observed in wildtype embryos, the
67 *wnt11f2* mutant formed a rod-like EP with a significant deficiency of the medio-lateral
68 dimension (Heisenberg, Brand et al. 1996, Heisenberg and Nusslein-Volhard 1997).
69 Another mutant kny*pek (kny)*, identified as having a nonsense mutation in *gpc4*, an
70 extracellular Wnt co-receptor, was identified as a gastrulation mutant that also exhibited
71 a shortened body axis due to a defect in embryonic convergent extension (CE) (Solnica-
72 Krezel, Stemple et al. 1996). In contrast to the *slb*/*wnt11f2 mutant*, the *gpc4* mutant
73 formed an EP that is wider in the medio-lateral dimension than the wildtype, in the
74 opposite end of the EP phenotypic spectrum compared to *wnt11f2* (Topczewski, Sepich
75 et al. 2001, Rochard, Monica et al. 2016). These observations beg the question of how
76 defects in early patterning and CE of the embryo may be associated with later
77 craniofacial morphogenesis. The observation that *wnt11f2* and *gpc4* mutant share
78 similar CE dysfunction and axis extension phenotypes but contrasting craniofacial
79 morphologies (Heisenberg and Nusslein-Volhard 1997) supports a hypothesis that CE
80 mechanisms regulated by these Wnt pathway genes are specific to the temporal and
81 spatial contexts during embryogenesis.
82
83 Dact (aka Frodo, Dapper) are scaffolding proteins that regulate Dishevelled (Dvl)-
84 mediated Wnt signaling, both positively and negatively (Cheyette, Waxman et al. 2002,
85 Gloy, Hikasa et al. 2002, Waxman, Hocking et al. 2004, Gao, Wen et al. 2008, Wen,

86 Chiang et al. 2010, Ma, Liu et al. 2015, Lee, Cheong et al. 2018). Dact proteins bind
87 directly to Dvl (Gloy, Hikasa et al. 2002, Brott and Sokol 2005, Lee, Cheong et al. 2018)
88 and interact with and inhibit members of TGF-β and Nodal signaling pathways (Zhang,
89 Zhou et al. 2004, Su, Zhang et al. 2007, Meng, Cheng et al. 2008, Kivimae, Yang et al.
90 2011). In chick and Xenopus, *Dact2* and *Dact1* (respectively) are expressed in the
91 neural folds during neural crest delamination and are important in epithelial-
92 mesenchymal transition (EMT), Wnt signaling, and TGF-β signaling (Hikasa and Sokol
93 2004, Schubert, Sobreira et al. 2014, Rabadan, Herrera et al. 2016). In mouse embryos,
94 Dact1 is expressed predominantly in mesodermal tissues, as well as ectodermal-
95 derived tissues, (Hunter, Hikasa et al. 2006) and ablation of Dact1 results in defective
96 EMT and primitive streak morphogenesis, with subsequent posterior defects (Wen,
97 Chiang et al. 2010). Mouse embryonic Dact2 expression has been described in the oral
98 epithelium and ablation of *Dact2* causes increased cell proliferation (Li, Florez et al.
99 2013) and re-epithelialization in mice (Meng, Cheng et al. 2008) and zebrafish (Kim,
100 Kim et al. 2020).
101
102 Previous experiments using morpholinos to disrupt *dact1* and *dact2* in zebrafish found
103 *dact1* morphants to be slightly smaller and to develop a normal body. In contrast, *dact2*
104 morphants were found to phenocopy described zebrafish gastrulation mutants, with
105 impaired CE, shortened body axis, and medially displaced eyes. Importantly, prior work
106 using morpholino-mediated gene disruption of *dact1* and *dact2* did not examine
107 craniofacial morphogenesis except to analyze *dact1* and *dact2* morphants head and eye
108 shapes under light microscopy (Waxman, Hocking et al. 2004). These experiments

109 were carried out at a time when morpholino was the accessible tool of gene disruption
110 (Nasevicius and Ekker 2000, Corey and Abrams 2001, Heasman 2002). Since
111 CRISPR/Cas9 targeted gene mutagenesis became popularized, many reports of
112 germline mutant phenotypes being discrepant from prior morpholino studies warranted
113 revisiting many of the prior work (Kok, Shin et al. 2015) and careful interpretation given
114 the caveats of each technology (Morcos, Vincent et al. 2015, Rossi, Kontarakis et al.
115 2015). More recently, a zebrafish CRISPR/Cas9 genetic *dact2* mutant has been
116 generated and studied, but unlike in the *dact2* morphant, no developmental phenotypes
117 were described (Kim, Kim et al. 2020).
118
119 Here we investigated the genetic requirement of *dact1* and *dact2* during embryogenesis
120 and craniofacial development using germline mutant alleles. We found an early
121 developmental role for *dact1* and *dact2* during gastrulation and body axis elongation.
122 We also characterized the abnormal craniofacial development of the *dact1/2* compound
123 mutants. We identified distinct transcriptomic profiles of wildtype, dact1/2, and gpc4
124 mutants during early development, including finding *calpain 8* (*capn8)* calcium-
125 dependent protease to be ectopically expressed in the *dact1/2* mutants. These results
126 elaborate on the cellular roles of dact1/2 and identify capn8 as a novel regulatory
127 candidate of embryogenesis.
128 **Results**
129 ***dact1* and *dact2* have distinct expression patterns throughout embryogenesis**
130 To determine the spatiotemporal gene expression of *dact1* and *dact2* during
131 embryogenesis we performed wholemount RNA *in situ* hybridization (ISH) across key

132 time points (Fig. 1). Given that the described craniofacial phenotypes of the *dact2*
133 morphant and the *wnt11f2* mutant are similar (Heisenberg and Nusslein-Volhard 1997,
134 Waxman, Hocking et al. 2004), we also performed *wnt11f2* ISH to compare to *dact1* and
135 *dact2* expression patterns.

136 During gastrulation at 8 hours post-fertilization (hpf; 75% epiboly), some regions
137 of *dact1* and *dact2* gene expression were shared and some areas are distinct to each
138 *dact* gene (Fig. 1A). Further, *dact* gene expression was distinct from *wnt11f2* in that
139 *wnt11f2* expression was not detected in the presumptive dorsal mesoderm. Transcripts
140 of *dact1*, *dact2,* and *wnt11f2* were all detected in the blastoderm margin, as previously
141 described (Makita, Mizuno et al. 1998, Heisenberg, Tada et al. 2000, Gillhouse, Wagner
142 Nyholm et al. 2004). Transcripts of *dact2*, and to a lesser extent *dact1*, were also
143 detected in the prechordal plate and chordamesoderm (Fig. 1A). Additionally, *dact2*
144 gene expression was concentrated in the shield and presumptive organizer or
145 Nieuwkoop center along with *wnt11f2*. This finding is consistent with previously
146 described expression patterns in zebrafish and supports a role for *dact1 and dact2* in
147 mesoderm induction and *dact2* in embryo dorsalization (Thisse 2001, Gillhouse,
148 Wagner Nyholm et al. 2004, Muyskens and Kimmel 2007, Oteiza, Koppen et al. 2010).
149 At the end of gastrulation and during somitogenesis the differences in the domains of
150 *dact1* and *dact2* gene expressions became more distinct (Fig. 1B,C). At tailbud stage,
151 *dact1* transcripts were detected in the neuroectoderm and the posterior paraxial
152 mesoderm, whereas *dact2* transcripts were detected in the anterior neural plate,
153 notochord, and tailbud. Anterior notochord and tailbud expression overlapped with
154 *wnt11f2* gene expression (Makita, Mizuno et al. 1998, Heisenberg, Tada et al. 2000).

155 The expression of *dact2* was unique in that its expression demarcated the anterior
156 border of the neural plate. As *dact2* morphants exhibited a craniofacial defect with
157 medially displaced eyes and midfacial hypoplasia (Waxman, Hocking et al. 2004), we
158 examined *dact1* and *dact2* expression in the orofacial tissues. At 24 hpf we found some
159 overlap but predominantly distinct expression patterns of *dact1* and *dact2* with *dact1*
160 being more highly expressed in the pharyngeal arches and *dact2* being expressed in
161 the midbrain/hindbrain boundary. Both *dact1* and *dact2* appeared to be expressed in the
162 developing oral cavity. At 48 hpf *dact1* expression is consistent with expression in the
163 developing craniofacial cartilage elements, while *dact2* expression appears within the
164 developing mouth. The distinct cellular expression profiles of *dact1* and *dact2* were
165 more clear in histological sections through the craniofacial region at 72 hpf. Utilizing
166 RNAscope *in situ* hybridization, we found that *dact2* and the epithelial gene *irf6* were co-
167 expressed in the surface and oral epithelium that surround the cartilaginous structures
168 (Fig. 1F). This is in contrast to *dact1* which was expressed in the developing cartilage of
169 the anterior neurocranium (ANC)/EP and palatoquadrate of the zebrafish larvae (Fig.
170 1F).

171 We examined the overall expression patterns of *dact1*, *dact2, gpc4,* and *wnt11f2*
172 using Daniocell single-cell sequencing data (Farrell, Wang et al. 2018). In general, we
173 found *dact1* spatiotemporal gene expression to be more similar to *gpc4* while *dact2*
174 gene expression was more similar to *wnt11f2* (Fig. S1). These results of shared but also
175 distinct domains of spatiotemporal gene expression of *dact1* and *dact2* suggest that the
176 *dact* paralogs may have some overlapping developmental functions while other roles
177 are paralog-specific.

178

179 ***dact1* and *dact2* contribute to axis extension and *dact1/2* compound mutants**

180 **exhibit a convergent extension defect**

181 *dact1* and *dact2* are known to interact with *disheveled* and regulate non-

182 canonical Wnt signaling (Gloy, Hikasa et al. 2002, Waxman, Hocking et al. 2004, Gao,

183 Wen et al. 2008, Wen, Chiang et al. 2010, Ma, Liu et al. 2015, Lee, Cheong et al. 2018)

184 and we have previously described the craniofacial anomalies of several zebrafish Wnt

185 mutants (Dougherty, Kamel et al. 2012, Kamel, Hoyos et al. 2013, Rochard, Monica et

186 al. 2016, Ling, Rochard et al. 2017, Alhazmi, Carroll et al. 2021). Previous work

187 investigated the effect of *dact1* and *dact2* disruption during zebrafish embryogenesis

188 using morpholinos and reported morphant phenotypes in embryonic axis extension and

189 eye fusion (Waxman, Hocking et al. 2004). However, the limitations associated with

190 morpholino-induced gene disruption (Kok, Shin et al. 2015, Morcos, Vincent et al. 2015,

191 Rossi, Kontarakis et al. 2015) and the fact that craniofacial morphogenesis was not

192 detailed for the *dact1* and *dact2* morphants, warranted the generation of mutant

193 germline alleles (Fig. S2). We created a *dact1* mutant allele (22 bp deletion, hereafter

194 *dact1-/-*) and a *dact2* mutant allele (7 bp deletion, hereafter *dact2-/-*), both resulting in a

195 premature stop codon and presumed protein truncation (Fig. S2A,B). Gene expression

196 of *dact1* and *dact2* was measured in pooled *dact1-/-*, *dact2-/-,* and *dact1/2-/-* embryos

197 (Fig. S2C). We found a decrease in *dact1* mRNA and an increase in *dact2* mRNA levels

198 in the respective CRISPR single mutants. We hypothesize that *dact2* mRNA levels are

199 maintained or elevated in the *dact2-/-* mutant due to the relative 3' position of the

200 deletion. In the *dact2-/-* embryos we found a slight increase in *dact1* mRNA levels,

201 suggesting a possible compensatory effect of dact2 disruption. The specificity of the
202 gene disruption was demonstrated by phenotypic rescue of the rod-like EP with the
203 injection of *dact1* or *dact2* mRNA. Injection of *dact1* mRNA or *dact2* mRNA or in
204 combination decreased the percentage of rod-like EP phenotype from near the
205 expected 25% (35% actual) to 2-7% (Fig. S2D,E).

206 Analysis of compound *dact1* and *dact2* heterozygote and homozygote alleles
207 during late gastrulation and early segmentation time points identified embryonic axis
208 extension anomalies (Fig. 2A,B). *dact1-/-* or *dact2-/-* homozygotes develop to be
209 phenotypically normal and viable. However, at 12 hpf, *dact2-/-* single mutants have a
210 significantly shorter body axis relative to wildtype. In contrast, body length shortening
211 phenotype was not observed in *dact1-/-* homozygotes. Compound heterozygotes of
212 *dact1+/-*; *dact2+/-* also developed normally but exhibited shorter body axis relative to
213 wildtype. The most significant axis shortening occurred in *dact1-/-; dact2-/-* double
214 homozygotes with a less severe truncation phenotype in the compound heterozygote
215 *dact1+/-; dact2-/-* (Fig. 2A,B). Interestingly, these changes in body axis extension do not
216 preclude the compound heterozygous larvae from reaching adulthood, except in the
217 *dact1-/-; dact2-/-* double homozygotes which did not survive from larval to juvenile
218 stages.

219 Body axis truncation has been attributed to impaired CE during gastrulation
220 (Tada and Heisenberg 2012). To delineate CE hallmarks in the *dact1*-/-;*dact2*-/-
221 mutants, we performed wholemount RNA ISH detecting genes that are expressed in
222 key domains along the body axis. At bud stage, *dact1-/-; dact2-/-* embryos demonstrate
223 bifurcated expression of *pax2a* and decreased anterior extension of *gsc* expression,

224 suggesting impaired midline convergence and anterior extension of the mesoderm (Fig.
225 2C). At the 1-2 somite stage, *zic1*, *pax2a* and *tbx6* are expressed in neural plate,
226 prospective midbrain and the tailbud, respectively, in both the wildtype and *dact1-/-;*
227 *dact2-/-* embryos. However, the spacing of these genes clearly revealed the shortening
228 of the anteroposterior body axis in the *dact1-/-; dact2-/-* embryos. Midline convergence
229 is decreased and the anterior border of the neural plate (marked by *zic1* expression)
230 was narrower in the *dact1-/-; dact2-/-* embryos (Fig. 2D). At the 10-somite stage (ss),
231 *dact1-/-; dact2-/-* embryos demonstrated decreased spacing between *ctslb1* and *pax2a*
232 gene expression, suggesting impaired lengthening of the anterior portion of the embryo.
233 Detection of muscle marker *myo1d* in the *dact1-/-; dact2-/-* embryos delineated impaired
234 posterior lengthening as well as reduced somitogenesis, evidenced by the decreased
235 number of somites (Fig. 2E). These data point to impaired CE of the mesoderm in
236 *dact1/2-/-* double mutants, which resulted in a shorter body axis. The aberrant CE and
237 axis extension in the *dact1/2*-/- phenotypes were similar to findings in other Wnt
238 mutants, such as *slb* and *kyn* (Heisenberg, Tada et al. 2000, Topczewski, Sepich et al.
239 2001) in that the body axis is truncated upon segmentation.
240

241 **_dact1_/_dact2_ compound mutants exhibit axis shortening and craniofacial**
242 **dysmorphology**

243 Given the defective converge phenotype and shortened axis in the *dact* mutants
244 during gastrulation, we examined the fish at 4 dpf for axis defects and for evidence of
245 defective morphogenesis in the craniofacial cartilages. Craniofacial morphology is an
246 excellent model for studying CE morphogenesis as many craniofacial cartilage elements

247 develop through this cellular mechanism (Kamel, Hoyos et al. 2013, Mork and Crump
248 2015, Sisson, Dale et al. 2015, Rochard, Monica et al. 2016). No craniofacial phenotype
249 was observed in *dact1* or *dact2* single mutants (data not shown). However, in-crossing
250 to generate *dact1/2-/-* compound homozygotes resulted in dramatic craniofacial
251 malformation (Fig. 3). Specificity of this phenotype to *dact1/2* was confirmed via rescue
252 with *dact1* or *dact2* mRNA injection (Fig. S2D,E). The *dact1/2-/-* mutant embryos
253 exhibited fully penetrant midfacial hypoplasia (Fig. 3A) however the degree of eye field
254 convergence in the midline varied between individuals. The forebrain protruded dorsally
255 and the mouth opening and ventral cartilage structures were displaced ventrally (Fig.
256 3A). Alcian blue staining of cartilage elements revealed severe narrowing of the EP into
257 a rod-like structure in 100 percent of double mutants, while the ventral cartilage
258 elements were largely unaffected (Fig. 3B). Notably the trabeculae extending posteriorly
259 from the EP and the rest of the posterior neurocranium exhibit wildtype morphology in
260 *dact1/2*. This *dact1/2-/-* double mutant phenotype is highly similar to that described for
261 *wnt11f2* (*slb*) mutants, a key regulator of non-canonical Wnt signaling and CE (Kimmel,
262 Miller et al. 2001).

263 As axis lengthening was found to be affected by loss of *dact1* and *dact2* (Fig. 2A)
264 we measured body length in 5 dpf *dact1/2* compound mutants. Using the length of the
265 vertebral spine as a measure of body length we found a trend (p=0.06) towards an
266 effect of *dact1* and *dact2* on shortening of the body length. Similar to axis length during
267 gastrulation/segmentation, the shortening was most pronounced in *dact1/2-/-* double
268 homozygous mutants versus wildtype clutch-mates (Fig. 3C, Fig. S3A,B).

269 As *wnt11f2* signals via disheveled and since dact proteins are known to interact
270 with disheveled (Wong, Bourdelas et al. 2003, Zhang, Gao et al. 2006, Kivimae, Yang et
271 al. 2011), it is suspected that dact has a role in wnt11f2 signaling. Combinatorial gene
272 disruption with morpholinos showed that *dact2* morpholino exasperated the *wnt11*
273 morpholino midfacial/eye fusion defect (Waxman, Hocking et al. 2004). We
274 hypothesized that the shared phenotypes between *wnt11f2* and *dact1/2* mutants point
275 to these genes acting in the same signaling pathway. To test for genetic epistasis
276 between *wnt11f2*, *dact1,* and *dact2* genes we generated *wnt11f2/dact1/2-/-* triple
277 homozygous mutants. If *wnt11f2* and *dact1/2* had independent developmental
278 requirements, the *wnt11f2/dact1/2-/-* mutant may exhibit a phenotype distinct from
279 *wnt11f2-/-* or *dact1/2-/-* mutants. We found that the *wnt11f2/dact1/2-/-* triple
280 homozygous mutant phenotype of the linear rod-like EP was the same as the *wnt11f2-/-*
281 mutant or *dact1/2-/-* double mutant, without exhibiting additional or neo-phenotypes in
282 the craniofacial cartilages or body axis (Fig. 3D,E). This result supports *dact1 and dact2*
283 acting downstream of *wnt11f2* signaling during ANC morphogenesis, where loss of
284 *dact1/2* function recapitulates a loss of *wnt11f2* signaling.
285
286 **Lineage tracing of *dact1/2* mutant NCC movements reveals their ANC**
287 **composition**
288 The EP forms from the convergence of a central frontal prominence-derived
289 structure with bilateral maxillary prominence-derived elements (Wada, Javidan et al.
290 2005, Swartz, Sheehan-Rooney et al. 2011, Dougherty, Kamel et al. 2012, Mork and
291 Crump 2015, Rochard, Monica et al. 2016).The stereotypic convergent migration of

292 cranial neural crest cells and their derivatives presents an excellent model to examine
293 CE movements and their effects on tissue morphogenesis. The zebrafish EP is formed
294 from the joining of a midline frontal prominence derived from the anteromost cranial
295 neural crest cell (NCC) population that migrate over the eyes and turn caudally, to join
296 paired lateral maxillary prominences derived from the second stream of cranial NCC
297 population that migrate rostrally (Kimmel, Miller et al. 2001, Wada, Javidan et al. 2005,
298 Schilling and Le Pabic 2009, Dougherty, Kamel et al. 2012, Mork and Crump 2015). The
299 EP that forms is a planar fan-shaped structure where we and others have shown that
300 the morphology is governed by Wnt signaling (Kimmel, Miller et al. 2001, Rochard,
301 Monica et al. 2016).

302 Given the rod-like EP we observed in the *dact1/2-/-* double mutants, we
303 hypothesized that the dysmorphology could be due to aberrant migration of the
304 anteromost midline stream of cranial NCCs resulting in fusion of the lateral maxillary
305 components. Conversely, an abrogated contribution from the second paired stream of
306 maxillary NCCs could lead to an EP composed entirely of the medial component. To
307 distinguish between these possibilities, we carried out lineage tracing
308 of the cranial NCC populations in wildtype and *dact1/2* mutants. The *dact1/2*
309 compound mutants were bred onto a *sox10:kaede* transgenic background, where we
310 and others have shown that the *sox10* reporter is a reliable driver of cranial neural crest
311 labeling (Wada, Javidan et al. 2005, Dutton, Antonellis et al. 2008, Swartz, Sheehan-
312 Rooney et al. 2011, Dougherty, Kamel et al. 2012, Kague, Gallagher et al. 2012, Mork
313 and Crump 2015). Cranial NCC populations in wildtype and *dact1/2* mutants were
314 targeted at 19 hpf to photoconvert Kaede reporter protein in either the anterior cranial

315 NCCs that contribute to the frontal prominence, or the second stream of NCCs that
316 contribute to the maxillary prominence, where the labeled cells were followed
317 longitudinally over 4.5 days of development (Fig. 4). We found that the anterior NCCs of
318 wildtype embryos migrated antero-dorsally to the eye and populated the medial EP. To
319 our surprise, the anterior cranial NCC also migrated to contribute to the median element
320 of the rod-like EP, suggesting the complex anterior then caudal migration of the anterior
321 NCC is not disrupted by *dact1/2* mutation (Fig. 4A, arrows). This finding is in contrast to
322 lineage tracing in another midline mutant with a similarly shaped rod-like EP, the *syu*
323 (*sonic hedgehog* null) mutant, where the anterior NCCs failed to populate the ANC
324 (Wada, Javidan et al. 2005).
325 Next, the second stream of NCC population that contribute to the maxillary
326 prominence was labeled, where they migrate and contribute to the lateral element of the
327 EP as expected in the wildtype (Fig. 4B). When the second stream of cranial NCCs
328 were labeled and followed in the *dact1/2* mutants, the cells were found to migrate
329 normally up to 36 hpf, but did not ultimately populate the EP in the mutant (arrows).
330 These results suggest that NCC migration itself is not regulated by *dact1/2* but that loss
331 of *dact1/2* hinders the second stream of NCCs' ability to populate the ANC by an
332 alternative means. Further, we have found that a rod-like EP can be formed from 2
333 different NCC origins, where in the *dact1/2* mutants the EP is contributed by the
334 anteromost frontonasal NCCs, in contrast to the similar rod-shaped EP of the *syu*
335 mutants that is formed from the more posterior stream of maxillary NCCs (Wada,
336 Javidan et al. 2005).
337

338 **Genetic interaction of *dact1/2* with *gpc4* and *wls* to determine facial morphology**

339 Given the role of Dact/dapper as modifiers of Wnt signaling, we hypothesized
340 that genetic interaction of *dact1/2* with *wls* and *gpc4* will modify facial morphology. Gpc4
341 is a glycoprotein that binds Wnt ligands and modulates Wnt signaling. *gpc4* zebrafish
342 mutants have impaired CE which leads to a shortened body axis (Topczewski, Sepich
343 et al. 2001). Wls is a posttranslational modifier of Wnt ligands which promotes their
344 secretion (Banziger, Soldini et al. 2006, Bartscherer, Pelte et al. 2006). We previously
345 described that these components of the Wnt/PCP pathway (*gpc4* receptor, *wls*
346 intracellular ligand chaperon, and Wnt ligands *wnt9a* and *wnt5b)* are required for
347 craniofacial morphogenesis, where each gene affects particular morphologic aspects of
348 chondrocytes arrangement in the cardinal axis of the ANC and Meckel's cartilage
349 (Rochard, Monica et al. 2016, Ling, Rochard et al. 2017). Using the EP as a
350 morphologic readout, we examined the genetic interaction of *dact1* and *dact2* with *wls*
351 and *gpc4*. Compound mutants of *dact1*, *dact2, gpc4* or *wls* were generated by breeding
352 the single alleles. Compared to wildtype ANC morphology, abrogation of *gpc4* led to
353 increased width in the transverse axis, but shorter in the antero-posterior axis (Rochard,
354 Monica et al. 2016). Disruption of *wls* leads to ANC morphology that is also wider in the
355 transverse dimension, but to a lesser degree than observed in *gpc4*. Additionally, in the
356 *wls* mutant, chondrocytes stack in greater layers in the sagittal axis (Rochard, Monica et
357 al. 2016).

358 Disruption of *gpc4* or *wls* in addition to *dact1/2* generated EP morphology that
359 contained phenotypic attributes from each single mutant, so that the resultant ANC
360 morphology represented a novel ANC form. The EP of a triple homozygous

361 *gpc4/dact1/2-/-* mutant was triangular, wider in the transverse axis and shorter in the
362 antero-posterior axis compared to the rod-like ANC observed in the *dact1/2-/-* double
363 mutant (Fig. 5A,B). Similarly, the ANC of a triple homozygous *wls/dact1/2-/-* mutant was
364 in the shape of a rod, shorter in the antero-posterior axis and thicker in the sagittal axis
365 compared to the *dact1/2-/-* double mutant, reflecting attributes of the *wls* mutant (Fig.
366 5C,D). In addition to the EP phenotypes, the triple homozygous *gpc4/dact1/2-/-* mutant
367 also had a short body axis and truncated tail similar but more severe than the *gpc4*
368 mutant (Fig. 5A). Since compound disruption of *dact1*, *dact2*, and *gpc4* or *wls* resulted
369 in a new phenotype we conclude that these genes function in different components of
370 Wnt signaling during craniofacial development.

371 As we analyzed the subsequent genotypes of our *dact1/dact2/gpc4* triple
372 heterozygote in-cross we gleaned more functional information about *dact1* and *dact2.*
373 We found that *dact1* heterozygosity in the context of *dact2-/-; gpc4-/-* was sufficient to
374 replicate the triple *dact1/dact2/gpc4* homozygous phenotype (Fig. 5E). In contrast,
375 *dact2* heterozygosity in the context of *dact1-/-; gpc4-/-* double mutant produced ANC in
376 the opposite phenotypic spectrum of ANC morphology, appearing similar to the *gpc4-/-*
377 mutant phenotype (Fig. 5E). These results show that *dact1* and *dact2* do not have
378 redundant function during craniofacial morphogenesis, and that *dact2* function is more
379 indispensable than *dact1*. These results also suggest that *dact1* and *gpc4* may have
380 overlapping roles in craniofacial development.

381

382 **_dact1/2_ and _gpc4_ regulate axis extension via overlapping and distinct cellular**
383 **pathways**

384 Our analyses of axis extension and the hallmarks of a CE defect (namely
385 decreased length and increased width between early tissues) demonstrate that *dact1*
386 and/or *dact2* are required for CE and anterior-posterior axis lengthening during
387 gastrulation (Fig. 3). An axis lengthening and CE defect has also been described in
388 *gpc4* (aka kny) mutants (Topczewski, Sepich et al. 2001). We also observe a defect in
389 axis lengthening in *gpc4-/-* in our hands (representative image Fig. 6A) that is grossly
390 similar to the *dact1/2-/-* mutants. Interestingly, the midfacial hypoplasia of the *wnt11f2*
391 (slb) mutant has been attributed to a defect in axis extension and anterior neural plate
392 patterning (Heisenberg and Nusslein-Volhard 1997), whereas defective axis extension
393 does not lead to midfacial hypoplasia in the *gpc4-/-* mutant. Therefore, we hypothesized
394 that by comparing and contrasting the gene expression changes in *dact1/2* versus *gpc4*
395 mutants during axis extension we could identify cell programs specifically responsible
396 for the anterior axis defect and subsequent midfacial hypoplasia. We performed single-
397 cell transcriptional analysis to compare *dact1/2* mutants, *gpc4* mutants, and wildtype
398 embryos during the segmentation stage. Single-cell encapsulation and barcoded cDNA
399 libraries were prepared from individual dissociated 4 ss wildtype, *dact1/2-/-* compound
400 mutant and *gpc4-/-* mutant embryos using the 10X Genomics Chromium platform and
401 Illumina next-generation sequencing. Genotyping of the embryos was not possible but
402 quality control analysis by considering the top 2000 most variable genes across the
403 dataset showed good clustering by genotype, indicating the reproducibility of individuals
404 in each group. Twenty clusters were identified using Louvain clustering and identity
405 was assigned by reviewing cluster-specific markers in light of published expression data
406 (Farrell, Wang et al. 2018, Farnsworth, Saunders et al. 2020, Bradford, Van Slyke et al.

407 2022) (Fig. 6B,C). Qualitatively, we did not observe any significant difference in cluster
408 abundance between genotype groups (Fig. S4). We found that *dact1*, *dact2*, and *gpc4*
409 were detected at various levels across clusters, though *dact1* expression was lower
410 than *dact2* (Fig. 6D), consistent with what we observed in RNA wholemount ISH
411 analysis (Fig. 1).

412 To assess the relative differences in gene expression between genotype groups,
413 we merged clusters into broader cell lineages: ectoderm, axial mesoderm, and paraxial
414 mesoderm (Fig. 7A). We focused on these cell types because they contribute
415 significantly to CE processes and axis establishment. For each of these cell lineages,
416 we performed independent pseudo-bulk differential expression analyses (DEA) of
417 wildtype vs. *dact1/2-/-* mutant and wildtype vs. *gpc4-/-* mutant (Fig. 7A). In all 3 cases,
418 we found differentially expressed genes (DEGs) that were commonly in *dact1-/-;dact2-/-*
419 and *gpc4-/-* mutant relative to wildtype (Fig. 7B). To address the hypothesis that *dact1*
420 and *dact2* regulate molecular pathways distinct from those regulated by *gpc4* we also
421 identified genes that were differentially expressed only in *dact1/2-/-* mutants or only in
422 *gpc4-/-* mutants (Fig. 7B). Functional analysis of these DEGs found unique enrichment
423 of intermediate filament genes in *gpc4-/-* whereas *dact1/2-/-* mutants had enrichment for
424 pathways associated with proteolysis (Fig. 7C, S5). Enrichment for pathways associated
425 with calcium-binding were found in both *gpc4-/-* and *dact1/2-/-*, although the specific
426 DEGs were distinct (Fig. S5). We performed functional analyses specifically for genes
427 that were differentially expressed in *dact1/2-/-* mutants, but not in *gpc4-/-* mutants, and
428 found enrichment in pathways associated with proteolysis (Fig. 7C) suggesting a novel
429 role for Dact in embryogenesis.

430 Interrogation of *dact1/2-/-* mutant-specific DEGs found that the calcium-
431 dependent cysteine protease *calpain 8* (*capn8*) was significantly overexpressed in
432 *dact1/2-/-* mutants in paraxial mesoderm (103 fold), axial mesoderm (33 fold), and in
433 ectoderm (3 fold; Fig. 7A). We also found that loss of *dact1/2* causes significant
434 changes to *capn8* expression pattern (Fig. 8A). Whereas *capn8* gene expression is
435 principally restricted to the epidermis of wildtype embryos, loss of *dact1/2* leads to
436 significant expansion of ectopic *capn8* gene expression in broader cell types such as in
437 mesodermal tissues (Fig. 8A). We corroborated this finding with wholemount RNA ISH
438 for *capn8* expression in wildtype versus *dact1/2*-/- 12 hpf embryos (Fig. 8B). The
439 expression of *smad1* was found to be decreased uniquely in the ectoderm of *dact1/2*-/-
440 embryos relative to wildtype (Fig. 7A), however this finding was not investigated further,
441 *Capn8* is considered a "classical" calpain, with domain homology similar to
442 *Capn1* and *Capn2* (Macqueen and Wilcox 2014). In adult human and mouse tissue,
443 *Capn8* expression is largely restricted to the gastrointestinal tract (Sorimachi, Ishiura et
444 al. 1993, Macqueen and Wilcox 2014), however embryonic expression in mammals has
445 not been characterized. Proteolytic targets of Capn8 have not been identified, however,
446 other classical calpains have been implicated in Wnt and cell-cell/ECM signaling
447 (Konze, van Diepen et al. 2014), including in Wnt/Ca^{+2} regulation of CE in Xenopus
448 (Zanardelli, Christodoulou et al. 2013). To determine whether the *dact1/2-/-* mutant
449 craniofacial phenotype could be attributed to *capn8* overexpression, we performed
450 injection of *capn8* or *gfp* control mRNA into 1 cell-stage zebrafish embryos. In wildtype
451 zebrafish, exogenous *capn8* mRNA caused the distinct *dact1/2*-/- craniofacial
452 phenotype including a rod-like ANC at a very low frequency (1 in 142 injected embryos).

453 This craniofacial phenotype was not observed in wildtype larvae, or when wildtype
454 embryos were injected with an equal concentration of *gfp* mRNA (0 in 192 injected
455 embryos) (data not shown). When mRNA was injected into 1 cell-stage embryos
456 generated from *dact1/2*+/- interbreeding, *capn8* caused a significant increase in the
457 number of larvae with the mutant craniofacial phenotype when on a *dact1/2*+/- genetic
458 background (Fig. 8D, 0.0% vs. 7.5%). We did not find an effect of exogenous *capn8* on
459 any other genotype, including *dact1-/-,dact2+/-* which we suspect to be due to the
460 smaller number of those individuals in our experimental population. These findings
461 suggest a new contribution of capn8 to embryonic development as well as anterior
462 neural plate patterning and craniofacial development. Further, the regulation of *capn8*
463 by *dact* may be required for normal embryogenesis and craniofacial morphogenesis.
464

465 **Discussion**

466 In this study, we examined the genetic requirement of *dact1* and *dact2* during
467 early embryogenesis and craniofacial morphogenesis in zebrafish. Wnt signaling is
468 central to the orchestration of embryogenesis and numerous proteins have been
469 identified as modulators of Wnt signaling, including *Dact1* and *Dact2* (Cheyette,
470 Waxman et al. 2002). Several studies across *Xenopus*, zebrafish, and mouse have
471 ascribed roles to *dact1* and *dact2,* including both promoting and antagonizing Wnt
472 signaling, depending on the developmental context (Cheyette, Waxman et al. 2002,
473 Gloy, Hikasa et al. 2002, Waxman, Hocking et al. 2004, Gao, Wen et al. 2008, Wen,
474 Chiang et al. 2010, Ma, Liu et al. 2015, Lee, Cheong et al. 2018). Here, we show that
475 *dact1* and *dact2* are required for axis extension during gastrulation and show an

476 example of CE defects during gastrulation associated with craniofacial defects. During
477 axis extension, we show that genetic disruption of *dact2,* but not *dact1,* resulted in a
478 significantly shortened axis relative to wildtype. This result is similar to what was
479 previously found using morpholinos to disrupt *dact1* and *dact2*. Interestingly, genetically
480 disrupted mutants of *dact1* or *dact2* developed to be phenotypically normal whereas
481 *dact1/2* compound mutants displayed a severe dysmorphic craniofacial phenotype.
482 Again, this is largely similar to the previous morpholino study that found disruption of
483 each gene to cause only a slight and occasional dysmorphic cranial phenotype at 24 hpf
484 (Waxman, Hocking et al. 2004). Notably, embryos injected with a mixture of *dact1* and
485 *dact2* morpholino were not characterized after 10 ss, and the singly injected embryos
486 were not characterized after 24 hpf (Waxman, Hocking et al. 2004). Therefore, by
487 analyzing genetic mutants of dact1 and dact2 our findings have largely validated the
488 previous morpholino literature as well as added new data on later developmental
489 outcomes.

490 The gene expression and genetic epistasis experiments carried out here support
491 that the *dact* paralogs are not redundant and have unique functions during different
492 stages of embryonic and larval development. We observed that *dact1* and *dact2* have
493 distinct spatiotemporal expression patterns throughout embryogenesis, suggesting
494 unique roles for each paralog in developmental processes. Differential expression of
495 *Dact1* and *Dact2* was also described during odontogenesis in mice (Kettunen, Kivimae
496 et al. 2010). This aligns with previous findings of differential roles of *dact1* and *dact2* in
497 canonical vs. non-canonical Wnt signaling (Waxman, Hocking et al. 2004) and a specific
498 role for *dact2*, but not *dact1*, in TGF-β signaling (Su, Zhang et al. 2007, Schubert,

499 Sobreira et al. 2014). However, the lack of a resultant phenotype upon genetic ablation
500 of *dact1* or *dact2* individually suggests the capability of functional compensation. This is
501 puzzling given their distinct expression patterns and needs to be examined further.
502 We found that *dact1* and *dact2* contribute to axis extension, and their compound
503 mutants exhibit a shortened and widened body axis that is consistent with a CE defect
504 during gastrulation. This finding aligns with previous studies that have implicated *dact1*
505 and *dact2* in non-canonical Wnt signaling and regulation of embryonic axis extension
506 (Waxman, Hocking et al. 2004). Based on our gene expression and combinatorial
507 genetic analyses, we offer the hypothesis that *dact1* expression in the paraxial
508 mesoderm is required for dorsal CE during gastrulation through its role in noncanonical
509 Wnt/PCP signaling, similar to the defect observed upon *gpc4* disruption. Conversely, we
510 posit that *dact2* functions in the prechordal mesoderm to promote anterior migration
511 during gastrulation, a function which has also been ascribed to *wnt11f2* (Heisenberg
512 and Nusslein-Volhard 1997). It is only upon loss of both *dact1* and *dact2* functions that
513 the axis is significantly truncated and a craniofacial malformation results. Further
514 experiments with spatially restricted gene ablation or cell transplantation are required to
515 test this hypothesis.
516 Our results underscore the crucial roles of *dact1* and *dact2* in embryonic
517 development and suggest a connection between gastrulation movements and
518 subsequent craniofacial morphogenesis. Our finding that in *dact1-/-;dact2-/-* compound
519 mutants the first stream of cranial NCC migrate and contribute to the ANC, while the
520 second stream fails to contribute suggests the possibility of an anatomical barrier to
521 migration, rather than an autonomous defect of the cranial NCCs. Disruption of the

522 sonic hedgehog signaling pathway in zebrafish results in a similar phenotype to *dact1/2-*
523 */-* and *wnt11f2-/-* mutants where the eyes converge medially and the EP narrows to a
524 rod shape. Interestingly, lineage tracing analysis in hedgehog-disrupted embryos found
525 the rod-like EP to consist solely of second stream-derived cranial NCCs (Wada, Javidan
526 et al. 2005). This is in contrast to the *dact1/2-/-* mutants, demonstrating two different
527 cellular mechanisms that result in a similar anatomical dysmorphology. It will be
528 important to test the generality of this phenomenon and determine if other mutants with
529 craniofacial abnormalities have early patterning differences. Further, a temporally
530 conditional genetic knockout is needed to definitively test the connection between early
531 and later development.

532 By comparing the transcriptome across different Wnt genetic contexts, i.e. *gpc4-*
533 */-* with that of the *dact1/2-/-* compound mutant, we identified a novel role for *dact1/2* in
534 the regulation of proteolysis, with significant misexpression of *capn8* in the mesoderm of
535 *dact1/2-/-* mutants. Although at a very low frequency, ectopic expression of *capn8*
536 mRNA recapitulated the *dact1/2-/-* mutant craniofacial phenotype, suggesting that
537 inhibition of *capn8* expression in the mesoderm by dact is required for normal
538 morphogenesis. Genes involved in calcium ion binding were also differentially
539 expressed in the *dact1/2-/-* mutants and we predict that altering intracellular calcium
540 handling in conjunction with *capn8* overexpression would increase the frequency of the
541 recapitulated *dact1/2-/-* mutant phenotype.

542 Capn8 is described as a stomach-specific calpain and a role during
543 embryogenesis has not been previously described. Calpains are typically calcium-
544 activated proteases and it is feasible that Capn8 is active in response to Wnt/Ca^{2+}

545 signaling. A close family member, Capn2 has been found to modulate Wnt signaling by
546 degradation of beta-catenin (Zanardelli, Christodoulou et al. 2013, Konze, van Diepen et
547 al. 2014). Our findings suggest that dact-dependent suppression of *capn8* expression is
548 necessary for normal embryogenesis and craniofacial morphogenesis, further
549 expanding the functional repertoire of *dact1/2*. Continued research is required to test a
550 direct regulatory role of dacts on *capn8* expression. While our data suggests an
551 interaction between dact signaling and capn8 function, we did not find capn8
552 overexpression to be wholly sufficient to cause the rod-like EP phenotype, Further, we
553 did not test the necessity of *capn8* for craniofacial development in this study. This study
554 does however identify capn8 as a novel embryonic gene warranting further investigation
555 into its role during embryogenesis, with possible implications for known craniofacial or
556 other disorders. Recently, Capn8 has been implicated in EMT associated with cancer
557 metastasis (Zhong, Xu et al. 2022, Song, Cui et al. 2024) and Xenopus capn8 was
558 found to be required for cranial NCC migration (Cousin, Abbruzzese et al. 2011) which
559 further supports a role of *capn8* in cranial NCC migration and craniofacial
560 morphogenesis.

561 Another gene identified in our scRNA-seq data to be differentially expressed in
562 the *dact1/22-/-* but not the *gpc4-/-* embryos was *smad1*. Smad1 acts in the TGF-β
563 signaling pathway and dact2 has been described to inhibit TGF-β and Nodal signaling
564 by promoting the degradation of Nodal receptors (Zhang, Zhou et al. 2004, Su, Zhang et
565 al. 2007, Meng, Cheng et al. 2008, Kivimae, Yang et al. 2011). Zebrafish Nodal pathway
566 mutants (*cyc/ndr2*, *oep/tdgf1*, *sqt/ndr1*) exhibit medially displaced eyes (Hatta, Kimmel
567 et al. 1991, Brand, Heisenberg et al. 1996, Heisenberg and Nusslein-Volhard 1997,

568 Feldman, Gates et al. 1998, Zhang, Talbot et al. 1998) and it is robustly feasible that
569 dysregulation of TGF-β signaling in the *dact1/2*-/- mutant contributes to the craniofacial
570 phenotype. Future research will examine the role of *dact1* and *dact2* in the coordination
571 of Wnt and TGF-β signaling and the importance of this coordination in the context of
572 craniofacial development. Of note, Sonic Hedgehog (shh) signaling is a principal
573 regulator to the vertebrate midline (Chiang, Litingtung et al. 1996, Ribes, Balaskas et al.
574 2010), and important in the development of the zebrafish floorplate (Halpern, Hatta et al.
575 1997, Odenthal, van Eeden et al. 2000). Mutants with disrupted *shh* expression or
576 signaling (*cyc/ndr2*, *smo, oep/tdgf1*) exhibit medially displaced eyes similar to the
577 *dact1/2* mutants (Brand, Heisenberg et al. 1996, Chen, Burgess et al. 2001). We did not
578 find any genes within the sonic hedgehog pathway to be differentially expressed in
579 *dact1/2* mutants, though post-transcriptional interactions cannot be ruled out.
580 This study has uncovered the genetic requirement of *dact1* and *dact2* in
581 embryonic CE and craniofacial morphogenesis, delineated the genetic interaction with
582 Wnt genes and identified capn8 as a modifier of this process. Future work will delineate
583 the molecular differences across the different *dact1/2* and other Wnt mutants to further
584 identify determinants of craniofacial morphogenesis; and to connect these findings to
585 clinically important Wnt regulators of facial morphology and pathology.
586
587 **Methods**
588
589 **Animals and CRISPR/Cas9 targeted mutagenesis**

590 All animal husbandry and experiments were performed in accordance with approval
591 from Massachusetts General Hospital Institutional Animal Care and Usage Committee.
592 Zebrafish (*Danio rerio*) embryos and adults were maintained in accordance with
593 institutional protocols. Embryos were raised at 28.5 C in E3 medium (Carroll, Macias
594 Trevino et al. 2020) and staged visually and according to standardized developmental
595 timepoints (Westerfield 1993). All zebrafish lines used for experiments and gene editing
596 were generated from the Tubingen or AB strain. The *wnt11f2* mutant line and gpc4-/-
597 mutant line were obtained from Zebrafish International Resource Center (wnt11f2$^{tx226/+}$
598 and gpc4$^{hi1688Tg/+}$ respectively). The *wls*-/- mutant line was originally gifted to the lab and
599 independently generated, as previously described (Rochard, Monica et al. 2016). The
600 *sox10*:kaede transgenic line was previously generated and described by our lab
601 (Dougherty, Kamel et al. 2012).
602
603 CRISPR sgRNA guides were designed using computational programs ZiFiT Targeter
604 v4.2 (zifit.partners.org/ZiFit) (Sander, Zaback et al. 2007), crispr.mit.edu
605 (https://zlab.bio/guide-design-resouces) (Ran, Hsu et al. 2013), and ChopChop
606 (https://chopchop.cbu.uib.no) (Montague, Cruz et al. 2014) with traditional sequence
607 constraints. Guides were chosen that were predicted to give high efficiency and
608 specificity. Guides best meeting these parameters were selected in exon 2 of *dact1* and
609 exon 4 of *dact2*. No suitable gRNA with sufficient efficiency were identified for *dact2* 5'
610 of exon 4 and the resulting phenotype was reassuring compared to previous morpholino
611 published results. Guides for *dact1* and *dact2* and Cas9 protein were prepared and
612 microinjected into 1 cell-stage zebrafish embryos and founders were identified as

613 previously described (Carroll, Macias Trevino et al. 2020). Primers flanking the sgRNA
614 guide site were designed for genotyping and fragment analysis was performed on
615 genomic DNA to detect base pair insertion/deletion. Sanger sequencing was performed
616 to verify targeted gene mutation and confirm the inclusion of a premature stop codon.
617 *dact1* forward primer: TACAGAAGCTGCTGAAGTACCG, *dact1* reverse primer:
618 CCCTCTCTCAAAGTGTTTTGGT, *dact2* forward primer:
619 TGAAGAGCTCCACTCCCCTGT, *dact2* reverse primer:
620 GCAGTTGAGGTCCATTCAGC.
621

622 **RT qPCR analysis**

623 Pooled wildtype, *dact1*-/-, *dact2*-/-, and *dact1/2*-/- fish were collected and RNA extractions
624 were performed using RNeasy Mini Kit (Qiagen). cDNA was generated using High
625 Capacity cDNA Reverse Transcription Kit (ThermoFisher). Quantitative PCR (qPCR) was
626 performed using *dact1* (Dr03152516_m1) and *dact2* (Dr03426298_s1) TaqMan Gene
627 Expression Assays. Expression was normalized to 18S rRNA expression (
628 Hs03003631_g1). TaQman Fast Advanced master mix (ThermoFisher) and a
629 StepOnePlus Real-Time PCR system (Applied Biosystems) were used to measure
630 relative mRNA levels, which were calculated using the ddCT method.
631

632 **Microinjection of mRNA**

633 Template DNA for *in vivo* mRNA transcription was generated by PCR amplification of
634 the gene of interest from a zebrafish embryo cDNA library and cloning into pCS2+8
635 destination plasmid. mRNA for injection was generated using an *in vitro* transcription kit

636 (Invitrogen mMessage mMachine). One-cell stage zebrafish embryos were injected with
637 2 nL of mRNA in solution. To test genetic knockout specificity, 150 or 300 pg or dact1,
638 dact2 or dact1 and dact2 mRNA was injected. For capn8 overexpression analysis 200
639 pg or GFP or capn8 mRNA was injected. Following phenotyping analysis, genotypes
640 were determined by fragment analysis of *dact1* and *dact2* genotyping PCR products.
641

642 **Wholemount and RNAscope *in situ* hybridization**

643 Wholemount *in situ* hybridization was performed as previously described (Carroll,
644 Macias Trevino et al. 2020). Zebrafish embryonic cDNA was used as a template to
645 generate riboprobes. Primers were designed to PCR amplify the specific riboprobe
646 sequence with a T7 promoter sequence linked to the reverse primer. *In vitro*
647 transcription was performed using a T7 polymerase and DIG-labeled nucleotides
648 (Roche). RNAscope was performed on sectioned zebrafish larvae as previously
649 described (Carroll, Macias Trevino et al. 2020). Probes were designed by and
650 purchased from ACD Bio. Hybridization and detection was performed according to the
651 manufacturer's protocol. Sections were imaged using a confocal microscope (Leica
652 SP8) and z-stack maximum projections were generated using Fiji software.
653

654 **Alcian blue staining and imaging**

655 Alcian blue staining and imaging were performed at 4 dpf as previously described
656 (Carroll, Macias Trevino et al. 2020). Briefly, larvae were fixed in 4% v/v formaldehyde
657 overnight at 4°C. Larvae were dehydrated in 50% v/v ethanol and stained with Alcian
658 blue as described (Walker and Kimmel 2007). Whole and dissected larvae were imaged

659 in 3% w/v methylcellulose using a Nikon Eclipse 80i compound microscope with a Nikon
660 DS Ri1 camera. Z-stacked images were taken and extended depth of field was
661 calculated using NIS Element BR 3.2 software. Images were processed using Fiji
662 software. After image capture embryos were genotyped by PCR and fragment analysis.
663

664 **Axis measurements**

665 Compound *dact1+/-*; *dact2+/-* zebrafish were in-crossed and progeny were collected
666 from 2 separate clutches and fixed in 4% formaldehyde at approximately 8ss. Embryos
667 were individually imaged using a Zeiss Axiozoom stereoscope and processed for DNA
668 extraction and genotyping (Westerfield 1993). Images were analyzed using Fiji. A circle
669 was drawn to overlay the yolk and the geometric center was determined using the
670 function on Fiji. Using the Fiji angle tool, lines were drawn from the center point to the
671 anterior-most point of the embryo and from the center to the posterior-most point of the
672 embryo. The resulting inner angle of these lines was determined. Each angle
673 measurement was then calculated as a ratio to the average angle of the wildtype
674 embryos. ANOVA was performed to determine statistical significance, $p<0.05$.
675

676 **Lineage analysis of cranial NCCs**

677 Live embryos were mounted in 1% w/v low melt agarose and covered with E3 medium
678 containing 0.013% w/v tricaine. Wildtype control and dact1/2-/- compound mutants on a
679 Tg(*soxl0*:kaede) background were imaged on a Leica DMi8 confocal microscope and
680 photoconverted using the UV laser (404 nm) until the green kaede fluorescence
681 disappeared. For each embryo, one side was photoconverted and the contralateral side

682 served as an internal control. After photoconversion, embryos were removed from the
683 agarose and raised in E3 medium at 28.5 C until the required developmental timepoint,
684 at which time they were similarly re-mounted and re-imaged. Z-stacked images were
685 processed as maximum-intensity projections using Fiji software.
686
687 **Single-cell RNA sequencing (scRNA-seq)**
688 Single-cell transcriptomic analyses were performed on 10 zebrafish embryos, including
689 4 wildtype, 3 *dact1-/-;dact2-/-* compound mutant, and 3 *gpc4-/-* mutant embryos.
690 Embryos were collected at 4 ss with *dact1-/-,dact2-/-* and *gpc4-/-* mutants being
691 identified by their truncated body axis. Embryos were dechorionated with a short
692 (approximately 10 min) incubation in 1 mg/ml Pronase and then washed 3x in embryo
693 medium. Cell dissociation was performed with modifications as previously described
694 (Farrell, Wang et al. 2018). Each embryo was transferred to 50 μl DMEM/F12 media on
695 ice. To dissociate cells, media was replaced with 200 μl DPBS (without Ca^{2+} and Mg^{2+})
696 with 0.1% w/v BSA. Embryos were disrupted by pipetting 10x with a P200 pipette tip.
697 500 μl of DPBS + 0.1% BSA was added and cells were centrifuged at 300xg for 1 min.
698 Cell pellets were resuspended in 200 μl DPBS + 0.1% BSA and kept on ice. Just prior
699 to encapsulation, cells were passed through a 40 μm cell strainer, and cell counts and
700 viability were measured. After droplet encapsulation, barcoding, and library preparation
701 using the 10X Genomics Chromium Single Cell 3' kit (version 3), data were sequenced
702 on an Illumina NovaSeq 6000 sequencer.
703 FASTQ files were demultiplexed and aligned to the GRCz11 build of the
704 zebrafish genome using Cellranger (version 6.1.0) (Zheng, Terry et al. 2017). Raw

705 Cellranger count matrices were imported into R (version 4.1.2) using Seurat (version
706 4.1.0) (Hao, Hao et al. 2021). First, we reviewed data for quality and excluded any
707 droplet that did not meet all of the following criteria: (i) have at least 1,500 unique
708 molecular identifiers (UMIs), (ii) covering at least 750 distinct genes; (iii) have <5% of
709 genes mapping to the mitochondrial genome; and (iv) have a log10 of detected genes
710 per UMI >80%. After quality control, the dataset was also filtered to exclude genes with
711 a detection rate below 1 in 3,000 cells, leaving a total of 20,078 distinct genes
712 expressed across 19,457 cells for analysis.
713 The quality-controlled count data were normalized using Pearson's residuals
714 from the regularized negative binomial regression model, as implemented in
715 Seurat::SCTransfrom (Hafemeister and Satija 2019). When computing the SCT model,
716 the effect of the total number of UMIs and number of detected genes per cell were
717 regressed out. After normalization, the top 3,000 most variably expressed genes were
718 used to calculate principal components (PCs). Data were then integrated by source
719 sample using Harmony (version 0.1.0) (Korsunsky, Millard et al. 2019). A two-
720 dimensional uniform manifold approximation and projection (UMAP) (Becht, McInnes et
721 al. 2018) was then derived from the first 40 Harmony embeddings for visualization.
722 Using the integrated Harmony embeddings, clusters were defined with the Louvain
723 clustering method, as implemented within Seurat. A resolution of 0.3 was used for
724 cluster definition. Cluster identities were assigned by manually reviewing the results of
725 Seurat::FindAllMarkers, searching for genes associated to known developmental
726 lineages. Gene expression data for key markers that guided cluster identity assignment
727 were visualized using Seurat::DotPlot.

728 Following this detailed annotation, some clusters were grouped to focus
729 downstream analyses on 3 major lineages: ventral mesoderm (grouping cells from the
730 pronephros, vasculogenic/myeloid precursors, hematopoietic cells, heart primordium,
731 and cephalic mesoderm clusters), dorsal mesoderm (adaxial cells, segmental plate, and
732 paraxial mesoderm), ectoderm (CNS, mid/hindbrain boundary, spinal cord, and neural
733 crest). For those 3 lineages, single-cell level data were aggregated per sample and
734 cluster to perform pseudobulk differential expression analyses (DEA) contrasting
735 genotypes. Independent pairwise comparisons of *dact1-/-;dact2-/-* versus wildtype and
736 *gpc4-/-* vs wildtype were performed using DESeq2 (v1.34.0) (Love, Huber et al. 2014).
737 P-values were corrected for multiple testing using the default Benjamini-Hochberg
738 method; log2 fold change values were corrected using the apeglm shrinkage estimator
739 (Zhu, Ibrahim et al. 2019). Significance was defined as an adjusted p-value < 0.1 and
740 log2 fold change > 0.58 in absolute value. Heatmaps of the top most significant
741 differentially expressed genes were generated from the regularized log transformed
742 data using pheatmap (version 1.0.12). Overlap in significant genes across pairwise
743 comparisons were determined and visualized in Venn diagrams. Over-representation
744 analyses against the Gene Ontology (GO) database were ran using clusterProfiler
745 (version 4.2.2) (Wu, Hu et al. 2021), using as input the set of genes found to be
746 differentially expressed in the comparison of *dact1-/-;dact-/-* versus wildtype but not
747 *gpc4-/-* versus wildtype. Sequencing data have been deposited in GEO under accession
748 code GSE240264.
749
750 **Statistical analysis**

751 Analyses were performed using Prism Software (GraphPad) unless otherwise specified.
752 An unpaired Student's *t* test or one-way ANOVA with multiple comparisons was used as
753 indicated and a *P*-value <0.05 was considered significant. Graphs represent the mean
754 +/- the SEM and *n* represents biological replicates. For categorical data (normal vs.
755 mutant phenotype) a Fisher exact test was performed between *gfp* and *capn8* injected
756 embryos and the odds ratio was determined. The confidence interval was determined
757 by the Baptista-Pike method.
758

759 **Acknowledgments**

760 We thank Christoph Seiler, Adele Donohue and the Aqautics Facility team at Children's
761 Hospital of Philadelphia; and Jessica Bethoney at Massachusetts General Hospital
762 (MGH) for their excellent management of our zebrafish colonies and facilities. We thank
763 the MGH Next Generation Sequencing Core for cell encapsulation, cDNA library
764 preparation, and sequencing. Single-cell sequencing analysis was performed by the
765 Harvard Chan Bioinformatics Core. Work by A.J. was funded in part by the Harvard
766 Stem Cell Institute. We appreciate and acknowledge the generous funding support from
767 the Shriners Hospitals for Children. This work was supported by the National Institutes
768 of Health grant R01DE027983 to E.C.L.
769
770
771
772
773

774 **References**

775 Alhazmi, N., S. H. Carroll, K. Kawasaki, K. C. Woronowicz, S. A. Hallett, C. Macias Trevino, E. B. Li,
776 R. Baron, F. Gori, P. C. Yelick, M. P. Harris and E. C. Liao (2021). "Synergistic roles of Wnt
777 modulators R-spondin2 and R-spondin3 in craniofacial morphogenesis and dental
778 development." Sci Rep **11**(1): 5871.

779 Banziger, C., D. Soldini, C. Schutt, P. Zipperlen, G. Hausmann and K. Basler (2006). "Wntless, a
780 conserved membrane protein dedicated to the secretion of Wnt proteins from signaling cells."
781 Cell **125**(3): 509-522.

782 Bartscherer, K., N. Pelte, D. Ingelfinger and M. Boutros (2006). "Secretion of Wnt ligands
783 requires Evi, a conserved transmembrane protein." Cell **125**(3): 523-533.

784 Becht, E., L. McInnes, J. Healy, C. A. Dutertre, I. W. H. Kwok, L. G. Ng, F. Ginhoux and E. W.
785 Newell (2018). "Dimensionality reduction for visualizing single-cell data using UMAP." Nat
786 Biotechnol.

787 Bradford, Y. M., C. E. Van Slyke, L. Ruzicka, A. Singer, A. Eagle, D. Fashena, D. G. Howe, K. Frazer,
788 R. Martin, H. Paddock, C. Pich, S. Ramachandran and M. Westerfield (2022). "Zebrafish
789 information network, the knowledgebase for Danio rerio research." Genetics **220**(4).

790 Brand, M., C. P. Heisenberg, R. M. Warga, F. Pelegri, R. O. Karlstrom, D. Beuchle, A. Picker, Y. J.
791 Jiang, M. Furutani-Seiki, F. J. van Eeden, M. Granato, P. Haffter, M. Hammerschmidt, D. A. Kane,
792 R. N. Kelsh, M. C. Mullins, J. Odenthal and C. Nusslein-Volhard (1996). "Mutations affecting
793 development of the midline and general body shape during zebrafish embryogenesis."
794 Development **123**: 129-142.

795 Brott, B. K. and S. Y. Sokol (2005). "Frodo proteins: modulators of Wnt signaling in vertebrate
796 development." Differentiation **73**(7): 323-329.

797 Carroll, S. H., C. Macias Trevino, E. B. Li, K. Kawasaki, N. Myers, S. A. Hallett, N. Alhazmi, J.
798 Cotney, R. P. Carstens and E. C. Liao (2020). "An Irf6-Esrp1/2 regulatory axis controls midface
799 morphogenesis in vertebrates." Development **147**(24).

800 Chen, W., S. Burgess and N. Hopkins (2001). "Analysis of the zebrafish smoothened mutant
801 reveals conserved and divergent functions of hedgehog activity." Development **128**(12): 2385-
802 2396.

803 Cheyette, B. N., J. S. Waxman, J. R. Miller, K. Takemaru, L. C. Sheldahl, N. Khlebtsova, E. P. Fox,
804 T. Earnest and R. T. Moon (2002). "Dapper, a Dishevelled-associated antagonist of beta-catenin
805 and JNK signaling, is required for notochord formation." Dev Cell **2**(4): 449-461.

806 Chiang, C., Y. Litingtung, E. Lee, K. E. Young, J. L. Corden, H. Westphal and P. A. Beachy (1996).
807 "Cyclopia and defective axial patterning in mice lacking Sonic hedgehog gene function." Nature
808 **383**(6599): 407-413.

809 Clevers, H. and R. Nusse (2012). "Wnt/beta-catenin signaling and disease." Cell **149**(6): 1192-
810 1205.

811 Corey, D. R. and J. M. Abrams (2001). "Morpholino antisense oligonucleotides: tools for
812 investigating vertebrate development." Genome Biol **2**(5): REVIEWS1015.

813 Cousin, H., G. Abbruzzese, E. Kerdavid, A. Gaultier and D. Alfandari (2011). "Translocation of the
814 cytoplasmic domain of ADAM13 to the nucleus is essential for Calpain8-a expression and cranial
815 neural crest cell migration." Dev Cell **20**(2): 256-263.

816 Dougherty, M., G. Kamel, V. Shubinets, G. Hickey, M. Grimaldi and E. C. Liao (2012). "Embryonic
817 fate map of first pharyngeal arch structures in the sox10: kaede zebrafish transgenic model." J
818 Craniofac Surg **23**(5): 1333-1337.

819 Dutton, J. R., A. Antonellis, T. J. Carney, F. S. Rodrigues, W. J. Pavan, A. Ward and R. N. Kelsh
820 (2008). "An evolutionarily conserved intronic region controls the spatiotemporal expression of
821 the transcription factor Sox10." BMC Dev Biol **8**: 105.

822 Farnsworth, D. R., L. M. Saunders and A. C. Miller (2020). "A single-cell transcriptome atlas for
823 zebrafish development." Dev Biol **459**(2): 100-108.

824 Farrell, J. A., Y. Wang, S. J. Riesenfeld, K. Shekhar, A. Regev and A. F. Schier (2018). "Single-cell
825 reconstruction of developmental trajectories during zebrafish embryogenesis." Science
826 **360**(6392).

827 Feldman, B., M. A. Gates, E. S. Egan, S. T. Dougan, G. Rennebeck, H. I. Sirotkin, A. F. Schier and
828 W. S. Talbot (1998). "Zebrafish organizer development and germ-layer formation require nodal-
829 related signals." Nature **395**(6698): 181-185.

830 Gao, X., J. Wen, L. Zhang, X. Li, Y. Ning, A. Meng and Y. G. Chen (2008). "Dapper1 is a
831 nucleocytoplasmic shuttling protein that negatively modulates Wnt signaling in the nucleus." J
832 Biol Chem **283**(51): 35679-35688.

833 Gillhouse, M., M. Wagner Nyholm, H. Hikasa, S. Y. Sokol and Y. Grinblat (2004). "Two
834 Frodo/Dapper homologs are expressed in the developing brain and mesoderm of zebrafish."
835 Dev Dyn **230**(3): 403-409.

836 Gloy, J., H. Hikasa and S. Y. Sokol (2002). "Frodo interacts with Dishevelled to transduce Wnt
837 signals." Nat Cell Biol **4**(5): 351-357.

838 Hafemeister, C. and R. Satija (2019). "Normalization and variance stabilization of single-cell
839 RNA-seq data using regularized negative binomial regression." Genome Biol **20**(1): 296.

840 Halpern, M. E., K. Hatta, S. L. Amacher, W. S. Talbot, Y. L. Yan, B. Thisse, C. Thisse, J. H.
841 Postlethwait and C. B. Kimmel (1997). "Genetic interactions in zebrafish midline development."
842 Dev Biol **187**(2): 154-170.

843 Hammerschmidt, M., F. Pelegri, M. C. Mullins, D. A. Kane, M. Brand, F. J. van Eeden, M.
844 Furutani-Seiki, M. Granato, P. Haffter, C. P. Heisenberg, Y. J. Jiang, R. N. Kelsh, J. Odenthal, R. M.
845 Warga and C. Nusslein-Volhard (1996). "Mutations affecting morphogenesis during gastrulation
846 and tail formation in the zebrafish, Danio rerio." Development **123**: 143-151.

847 Hao, Y., S. Hao, E. Andersen-Nissen, W. M. Mauck, 3rd, S. Zheng, A. Butler, M. J. Lee, A. J. Wilk,
848 C. Darby, M. Zager, P. Hoffman, M. Stoeckius, E. Papalexi, E. P. Mimitou, J. Jain, A. Srivastava, T.
849 Stuart, L. M. Fleming, B. Yeung, A. J. Rogers, J. M. McElrath, C. A. Blish, R. Gottardo, P. Smibert
850 and R. Satija (2021). "Integrated analysis of multimodal single-cell data." Cell **184**(13): 3573-
851 3587 e3529.

852 Hashimoto, M., H. Morita and N. Ueno (2014). "Molecular and cellular mechanisms of
853 development underlying congenital diseases." Congenit Anom (Kyoto) **54**(1): 1-7.

854 Hatta, K., C. B. Kimmel, R. K. Ho and C. Walker (1991). "The cyclops mutation blocks
855 specification of the floor plate of the zebrafish central nervous system." Nature **350**(6316): 339-
856 341.

857 Heasman, J. (2002). "Morpholino oligos: making sense of antisense?" Dev Biol **243**(2): 209-214.

858 Heisenberg, C. P., M. Brand, Y. J. Jiang, R. M. Warga, D. Beuchle, F. J. van Eeden, M. Furutani-
859 Seiki, M. Granato, P. Haffter, M. Hammerschmidt, D. A. Kane, R. N. Kelsh, M. C. Mullins, J.
860 Odenthal and C. Nusslein-Volhard (1996). "Genes involved in forebrain development in the
861 zebrafish, Danio rerio." Development **123**: 191-203.

862 Heisenberg, C. P. and C. Nusslein-Volhard (1997). "The function of silberblick in the positioning
863 of the eye anlage in the zebrafish embryo." Dev Biol **184**(1): 85-94.

864 Heisenberg, C. P., M. Tada, G. J. Rauch, L. Saude, M. L. Concha, R. Geisler, D. L. Stemple, J. C.
865 Smith and S. W. Wilson (2000). "Silberblick/Wnt11 mediates convergent extension movements
866 during zebrafish gastrulation." Nature **405**(6782): 76-81.

867 Hikasa, H. and S. Y. Sokol (2004). "The involvement of Frodo in TCF-dependent signaling and
868 neural tissue development." Development **131**(19): 4725-4734.

869 Hunter, N. L., H. Hikasa, S. M. Dymecki and S. Y. Sokol (2006). "Vertebrate homologues of Frodo
870 are dynamically expressed during embryonic development in tissues undergoing extensive
871 morphogenetic movements." Dev Dyn **235**(1): 279-284.

872 Huybrechts, Y., G. Mortier, E. Boudin and W. Van Hul (2020). "WNT Signaling and Bone: Lessons
873 From Skeletal Dysplasias and Disorders." Front Endocrinol (Lausanne) **11**: 165.

874 Ji, Y., H. Hao, K. Reynolds, M. McMahon and C. J. Zhou (2019). "Wnt Signaling in Neural Crest
875 Ontogenesis and Oncogenesis." Cells **8**(10).

876 Kague, E., M. Gallagher, S. Burke, M. Parsons, T. Franz-Odendaal and S. Fisher (2012).
877 "Skeletogenic fate of zebrafish cranial and trunk neural crest." PLoS One **7**(11): e47394.

878 Kamel, G., T. Hoyos, L. Rochard, M. Dougherty, Y. Kong, W. Tse, V. Shubinets, M. Grimaldi and E.
879 C. Liao (2013). "Requirement for frzb and fzd7a in cranial neural crest convergence and
880 extension mechanisms during zebrafish palate and jaw morphogenesis." Dev Biol **381**(2): 423-
881 433.

882 Kettunen, P., S. Kivimae, P. Keshari, O. D. Klein, B. N. Cheyette and K. Luukko (2010). "Dact1-3
883 mRNAs exhibit distinct expression domains during tooth development." Gene Expr Patterns
884 **10**(2-3): 140-143.

885 Kim, D. H., E. J. Kim, D. H. Kim and S. W. Park (2020). "Dact2 is involved in the regulation of
886 epithelial-mesenchymal transition." Biochem Biophys Res Commun **524**(1): 190-197.

887 Kimmel, C. B., C. T. Miller and C. B. Moens (2001). "Specification and morphogenesis of the
888 zebrafish larval head skeleton." Dev Biol **233**(2): 239-257.

889 Kivimae, S., X. Y. Yang and B. N. Cheyette (2011). "All Dact (Dapper/Frodo) scaffold proteins
890 dimerize and exhibit conserved interactions with Vangl, Dvl, and serine/threonine kinases."
891 BMC Biochem **12**: 33.

892 Kok, F. O., M. Shin, C. W. Ni, A. Gupta, A. S. Grosse, A. van Impel, B. C. Kirchmaier, J. Peterson-
893 Maduro, G. Kourkoulis, I. Male, D. F. DeSantis, S. Sheppard-Tindell, L. Ebarasi, C. Betsholtz, S.
894 Schulte-Merker, S. A. Wolfe and N. D. Lawson (2015). "Reverse genetic screening reveals poor
895 correlation between morpholino-induced and mutant phenotypes in zebrafish." Dev Cell **32**(1):
896 97-108.

897 Konze, S. A., L. van Diepen, A. Schroder, R. Olmer, H. Moller, A. Pich, R. Weissmann, A. W. Kuss,
898 R. Zweigerdt and F. F. Buettner (2014). "Cleavage of E-cadherin and beta-catenin by calpain
899 affects Wnt signaling and spheroid formation in suspension cultures of human pluripotent stem
900 cells." Mol Cell Proteomics **13**(4): 990-1007.

901 Korsunsky, I., N. Millard, J. Fan, K. Slowikowski, F. Zhang, K. Wei, Y. Baglaenko, M. Brenner, P. R.
902 Loh and S. Raychaudhuri (2019). "Fast, sensitive and accurate integration of single-cell data
903 with Harmony." Nat Methods **16**(12): 1289-1296.

904 Lee, H., S. M. Cheong, W. Han, Y. Koo, S. B. Jo, G. S. Cho, J. S. Yang, S. Kim and J. K. Han (2018).
905 "Head formation requires Dishevelled degradation that is mediated by March2 in concert with
906 Dapper1." Development **145**(7).

907 Li, X., S. Florez, J. Wang, H. Cao and B. A. Amendt (2013). "Dact2 represses PITX2 transcriptional
908 activation and cell proliferation through Wnt/beta-catenin signaling during odontogenesis."
909 PLoS One **8**(1): e54868.

910 Ling, I. T., L. Rochard and E. C. Liao (2017). "Distinct requirements of wls, wnt9a, wnt5b and
911 gpc4 in regulating chondrocyte maturation and timing of endochondral ossification." Dev Biol
912 **421**(2): 219-232.

913 Logan, C. Y. and R. Nusse (2004). "The Wnt signaling pathway in development and disease."
914 Annu Rev Cell Dev Biol **20**: 781-810.

915 Loh, K. M., R. van Amerongen and R. Nusse (2016). "Generating Cellular Diversity and Spatial
916 Form: Wnt Signaling and the Evolution of Multicellular Animals." Dev Cell **38**(6): 643-655.

917 Love, M. I., W. Huber and S. Anders (2014). "Moderated estimation of fold change and
918 dispersion for RNA-seq data with DESeq2." Genome Biol **15**(12): 550.

919 Ma, B., B. Liu, W. Cao, C. Gao, Z. Qi, Y. Ning and Y. G. Chen (2015). "The Wnt Signaling
920 Antagonist Dapper1 Accelerates Dishevelled2 Degradation via Promoting Its Ubiquitination and
921 Aggregate-induced Autophagy." J Biol Chem **290**(19): 12346-12354.

922 Macqueen, D. J. and A. H. Wilcox (2014). "Characterization of the definitive classical calpain
923 family of vertebrates using phylogenetic, evolutionary and expression analyses." Open Biol **4**(4):
924 130219.

925 Makita, R., T. Mizuno, S. Koshida, A. Kuroiwa and H. Takeda (1998). "Zebrafish wnt11: pattern
926 and regulation of the expression by the yolk cell and No tail activity." Mech Dev **71**(1-2): 165-
927 176.

928 Mehta, S., S. Hingole and V. Chaudhary (2021). "The Emerging Mechanisms of Wnt Secretion
929 and Signaling in Development." Front Cell Dev Biol **9**: 714746.

930 Meng, F., X. Cheng, L. Yang, N. Hou, X. Yang and A. Meng (2008). "Accelerated re-
931 epithelialization in Dpr2-deficient mice is associated with enhanced response to TGFbeta
932 signaling." J Cell Sci **121**(Pt 17): 2904-2912.

933 Montague, T. G., J. M. Cruz, J. A. Gagnon, G. M. Church and E. Valen (2014). "CHOPCHOP: a
934 CRISPR/Cas9 and TALEN web tool for genome editing." Nucleic Acids Res **42**(Web Server issue):
935 W401-407.

936 Morcos, P. A., A. C. Vincent and J. D. Moulton (2015). "Gene Editing Versus Morphants."
937 Zebrafish **12**(5): 319.

938 Mork, L. and G. Crump (2015). "Zebrafish Craniofacial Development: A Window into Early
939 Patterning." Curr Top Dev Biol **115**: 235-269.

940 Muyskens, J. B. and C. B. Kimmel (2007). "Tbx16 cooperates with Wnt11 in assembling the
941 zebrafish organizer." Mech Dev **124**(1): 35-42.

942 Nasevicius, A. and S. C. Ekker (2000). "Effective targeted gene 'knockdown' in zebrafish." Nat
943 Genet **26**(2): 216-220.

944 Niehrs, C. (2012). "The complex world of WNT receptor signalling." Nat Rev Mol Cell Biol **13**(12):
945 767-779.

946 Odenthal, J., F. J. van Eeden, P. Haffter, P. W. Ingham and C. Nusslein-Volhard (2000). "Two
947 distinct cell populations in the floor plate of the zebrafish are induced by different pathways."
948 Dev Biol **219**(2): 350-363.

949 Oteiza, P., M. Koppen, M. Krieg, E. Pulgar, C. Farias, C. Melo, S. Preibisch, D. Muller, M. Tada, S.
950 Hartel, C. P. Heisenberg and M. L. Concha (2010). "Planar cell polarity signalling regulates cell
951 adhesion properties in progenitors of the zebrafish laterality organ." Development **137**(20):
952 3459-3468.

953 Petersen, C. P. and P. W. Reddien (2009). "Wnt signaling and the polarity of the primary body
954 axis." Cell **139**(6): 1056-1068.

955 Piotrowski, T., T. F. Schilling, M. Brand, Y. J. Jiang, C. P. Heisenberg, D. Beuchle, H. Grandel, F. J.
956 van Eeden, M. Furutani-Seiki, M. Granato, P. Haffter, M. Hammerschmidt, D. A. Kane, R. N.
957 Kelsh, M. C. Mullins, J. Odenthal, R. M. Warga and C. Nusslein-Volhard (1996). "Jaw and
958 branchial arch mutants in zebrafish II: anterior arches and cartilage differentiation."
959 Development **123**: 345-356.

960 Rabadan, M. A., A. Herrera, L. Fanlo, S. Usieto, C. Carmona-Fontaine, E. H. Barriga, R. Mayor, S.
961 Pons and E. Marti (2016). "Delamination of neural crest cells requires transient and reversible
962 Wnt inhibition mediated by Dact1/2." Development **143**(12): 2194-2205.

963 Ran, F. A., P. D. Hsu, J. Wright, V. Agarwala, D. A. Scott and F. Zhang (2013). "Genome
964 engineering using the CRISPR-Cas9 system." Nat Protoc **8**(11): 2281-2308.

965 Reynolds, K., P. Kumari, L. Sepulveda Rincon, R. Gu, Y. Ji, S. Kumar and C. J. Zhou (2019). "Wnt
966 signaling in orofacial clefts: crosstalk, pathogenesis and models." Dis Model Mech **12**(2).

967 Ribes, V., N. Balaskas, N. Sasai, C. Cruz, E. Dessaud, J. Cayuso, S. Tozer, L. L. Yang, B. Novitch, E.
968 Marti and J. Briscoe (2010). "Distinct Sonic Hedgehog signaling dynamics specify floor plate and
969 ventral neuronal progenitors in the vertebrate neural tube." Genes Dev **24**(11): 1186-1200.

970 Rochard, L., S. D. Monica, I. T. Ling, Y. Kong, S. Roberson, R. Harland, M. Halpern and E. C. Liao
971 (2016). "Roles of Wnt pathway genes wls, wnt9a, wnt5b, frzb and gpc4 in regulating
972 convergent-extension during zebrafish palate morphogenesis." Development **143**(14): 2541-
973 2547.

974 Rossi, A., Z. Kontarakis, C. Gerri, H. Nolte, S. Holper, M. Kruger and D. Y. Stainier (2015).
975 "Genetic compensation induced by deleterious mutations but not gene knockdowns." Nature
976 **524**(7564): 230-233.

977 Sander, J. D., P. Zaback, J. K. Joung, D. F. Voytas and D. Dobbs (2007). "Zinc Finger Targeter
978 (ZiFiT): an engineered zinc finger/target site design tool." Nucleic Acids Res **35**(Web Server
979 issue): W599-605.

980 Schilling, T. F. and P. Le Pabic (2009). "Fishing for the signals that pattern the face." J Biol **8**(11):
981 101.

982 Schubert, F. R., D. R. Sobreira, R. G. Janousek, L. E. Alvares and S. Dietrich (2014). "Dact genes
983 are chordate specific regulators at the intersection of Wnt and Tgf-beta signaling pathways."
984 BMC Evol Biol **14**: 157.

985 Shi, D. L. (2022). "Wnt/planar cell polarity signaling controls morphogenetic movements of
986 gastrulation and neural tube closure." Cell Mol Life Sci **79**(12): 586.

987 Sisson, B. E., R. M. Dale, S. R. Mui, J. M. Topczewska and J. Topczewski (2015). "A role of
988 glypican4 and wnt5b in chondrocyte stacking underlying craniofacial cartilage morphogenesis."
989 Mech Dev **138 Pt 3**: 279-290.

990 Solnica-Krezel, L., D. L. Stemple, E. Mountcastle-Shah, Z. Rangini, S. C. Neuhauss, J. Malicki, A. F.
991 Schier, D. Y. Stainier, F. Zwartkruis, S. Abdelilah and W. Driever (1996). "Mutations affecting cell
992 fates and cellular rearrangements during gastrulation in zebrafish." Development **123**: 67-80.

993 Song, N., K. Cui, L. Zeng, Y. Fan, Z. Wang, P. Shi, W. Su and H. Wang (2024). "Calpain 8 as a
994 potential biomarker regulates the progression of pancreatic cancer via EMT and AKT/ERK
995 pathway." J Proteomics **301**: 105182.

996 Sorimachi, H., S. Ishiura and K. Suzuki (1993). "A novel tissue-specific calpain species expressed
997 predominantly in the stomach comprises two alternative splicing products with and without
998 Ca(2+)-binding domain." J Biol Chem **268**(26): 19476-19482.

999 Steinhart, Z. and S. Angers (2018). "Wnt signaling in development and tissue homeostasis."
1000 Development **145**(11).

1001 Su, Y., L. Zhang, X. Gao, F. Meng, J. Wen, H. Zhou, A. Meng and Y. G. Chen (2007). "The
1002 evolutionally conserved activity of Dapper2 in antagonizing TGF-beta signaling." FASEB J **21**(3):
1003 682-690.

1004 Swartz, M. E., K. Sheehan-Rooney, M. J. Dixon and J. K. Eberhart (2011). "Examination of a
1005 palatogenic gene program in zebrafish." Dev Dyn **240**(9): 2204-2220.

1006 Tada, M. and C. P. Heisenberg (2012). "Convergent extension: using collective cell migration
1007 and cell intercalation to shape embryos." Development **139**(21): 3897-3904.

1008 Thisse, B., Pflumio, S., Furthauer, M., Loppin, B., Heyer, V., Degrave, A., Woehl, R., Lux, A.,
1009 Steffan, T., Charbonnier, X.Q., Thisse, C. (2001). "Expression of the zebrafish genome during
1010 embryogenesis." from http://zfin.org.

1011 Topczewski, J., D. S. Sepich, D. C. Myers, C. Walker, A. Amores, Z. Lele, M. Hammerschmidt, J.
1012 Postlethwait and L. Solnica-Krezel (2001). "The zebrafish glypican knypek controls cell polarity
1013 during gastrulation movements of convergent extension." Dev Cell **1**(2): 251-264.

1014 Wada, N., Y. Javidan, S. Nelson, T. J. Carney, R. N. Kelsh and T. F. Schilling (2005). "Hedgehog
1015 signaling is required for cranial neural crest morphogenesis and chondrogenesis at the midline
1016 in the zebrafish skull." Development **132**(17): 3977-3988.

1017 Walker, M. B. and C. B. Kimmel (2007). "A two-color acid-free cartilage and bone stain for
1018 zebrafish larvae." Biotech Histochem **82**(1): 23-28.

1019 Waxman, J. S., A. M. Hocking, C. L. Stoick and R. T. Moon (2004). "Zebrafish Dapper1 and
1020 Dapper2 play distinct roles in Wnt-mediated developmental processes." Development **131**(23):
1021 5909-5921.

1022 Wen, J., Y. J. Chiang, C. Gao, H. Xue, J. Xu, Y. Ning, R. J. Hodes, X. Gao and Y. G. Chen (2010).
1023 "Loss of Dact1 disrupts planar cell polarity signaling by altering dishevelled activity and leads to
1024 posterior malformation in mice." J Biol Chem **285**(14): 11023-11030.

1025 Westerfield, M. (1993). The zebrafish book : a guide for the laboratory use of zebrafish
1026 (Brachydanio rerio). Eugene, OR, M. Westerfield.

1027 Wiese, K. E., R. Nusse and R. van Amerongen (2018). "Wnt signalling: conquering complexity."
1028 Development **145**(12).

1029 Wong, H. C., A. Bourdelas, A. Krauss, H. J. Lee, Y. Shao, D. Wu, M. Mlodzik, D. L. Shi and J. Zheng
1030 (2003). "Direct binding of the PDZ domain of Dishevelled to a conserved internal sequence in
1031 the C-terminal region of Frizzled." Mol Cell **12**(5): 1251-1260.

1032 Wu, T., E. Hu, S. Xu, M. Chen, P. Guo, Z. Dai, T. Feng, L. Zhou, W. Tang, L. Zhan, X. Fu, S. Liu, X.
1033 Bo and G. Yu (2021). "clusterProfiler 4.0: A universal enrichment tool for interpreting omics
1034 data." Innovation (Camb) **2**(3): 100141.

1035 Zanardelli, S., N. Christodoulou and P. A. Skourides (2013). "Calpain2 protease: A new member
1036 of the Wnt/Ca(2+) pathway modulating convergent extension movements in Xenopus." Dev Biol
1037 **384**(1): 83-100.

1038 Zhang, J., W. S. Talbot and A. F. Schier (1998). "Positional cloning identifies zebrafish one-eyed
1039 pinhead as a permissive EGF-related ligand required during gastrulation." Cell **92**(2): 241-251.

1040 Zhang, L., X. Gao, J. Wen, Y. Ning and Y. G. Chen (2006). "Dapper 1 antagonizes Wnt signaling by
1041 promoting dishevelled degradation." J Biol Chem **281**(13): 8607-8612.

1042 Zhang, L., H. Zhou, Y. Su, Z. Sun, H. Zhang, L. Zhang, Y. Zhang, Y. Ning, Y. G. Chen and A. Meng
1043 (2004). "Zebrafish Dpr2 inhibits mesoderm induction by promoting degradation of nodal
1044 receptors." Science **306**(5693): 114-117.

1045 Zheng, G. X., J. M. Terry, P. Belgrader, P. Ryvkin, Z. W. Bent, R. Wilson, S. B. Ziraldo, T. D.
1046 Wheeler, G. P. McDermott, J. Zhu, M. T. Gregory, J. Shuga, L. Montesclaros, J. G. Underwood, D.
1047 A. Masquelier, S. Y. Nishimura, M. Schnall-Levin, P. W. Wyatt, C. M. Hindson, R. Bharadwaj, A.
1048 Wong, K. D. Ness, L. W. Beppu, H. J. Deeg, C. McFarland, K. R. Loeb, W. J. Valente, N. G. Ericson,
1049 E. A. Stevens, J. P. Radich, T. S. Mikkelsen, B. J. Hindson and J. H. Bielas (2017). "Massively
1050 parallel digital transcriptional profiling of single cells." Nat Commun **8**: 14049.

1051 Zhong, X., S. Xu, Q. Wang, L. Peng, F. Wang, T. He, C. Liu, S. Ni and Z. He (2022). "CAPN8 involves
1052 with exhausted, inflamed, and desert immune microenvironment to influence the metastasis of
1053 thyroid cancer." Front Immunol **13**: 1013049.

1054 Zhu, A., J. G. Ibrahim and M. I. Love (2019). "Heavy-tailed prior distributions for sequence count
1055 data: removing the noise and preserving large differences." Bioinformatics **35**(12): 2084-2092.
1056

1057

1058

1059

1060

1061

1062

1063

1064

1065

1066

1067

1068

1069

1070

1071

1072

1073 **Figure Legends**

1074

1075 **Figure 1**. Unique and shared *dact1* and *dact2* gene expression domains during
1076 zebrafish development. **(A-C)** Representative images of wholemount *in situ*
1077 hybridization showing *dact1*, *dact2,* and *wnt11f2* gene expression patterns. **A)** At 8 hpf,
1078 *dact2* and *wnt11f2* are highly expressed in the dorsal margin and presumptive
1079 Nieuwkoop center of the gastrulating embryo, with *dact1* being weakly detected
1080 (arrowhead). In contrast to *wnt11f2*, *dact1* and *dact2* are expressed in the presumptive
1081 dorsal mesoderm (asterisk). **B)** Lateral (anterior to the left of page) and anterior (dorsal
1082 side toward top of page) views of bud-stage embryos. *dact2* and *wnt11f2* transcripts are
1083 both detected in the tailbud (asterisk) while *dact2* is additionally expressed in the axial
1084 mesoderm (arrow). *dact1* gene expression is concentrated to the paraxial mesoderm
1085 and the neuroectoderm (open arrowheads). **C)** Lateral and flat-mount views of 4 ss
1086 embryos. *dact2* is expressed in the anterior neural plate and polster (P), notochord (N),
1087 paraxial and presomitic mesoderm (PM) and tailbud (TB). In contrast, *dact1* is
1088 expressed in the midbrain (MB) and the paraxial and presomitic mesoderm. (**D-E)**
1089 Representative lateral (anterior to left of page) images of wholemount *in situ*
1090 hybridization showing *dact1* and *dact2* expression patterns. **D)** At 24 hpf expression is
1091 detected in the developing head. **E)** At 48 hpf expression is detected in the developing
1092 craniofacial structures (arrow). **F)** Representative images of RNAscope *in situ*
1093 hybridization analysis of *dact1* (white) and *dact2* (yellow) and *irf6* (green) expression in
1094 transverse section of 72 hpf embryos. *dact1* is expressed in the ethmoid plate (ep) and
1095 palatoquadrate (pq) orofacial cartilage, while *dact2* is expressed in the oral epithelium

1096 (oe). The epithelial marker *irf6* is expressed in the oe and surface epithelium (se). Dapi
1097 (blue). Scale bar: 100 μm.
1098
1099 **Figure 2**. Impaired convergent extension in *dact1/2* compound mutants. **A)** Inter-cross
1100 of compound heterozygotes yield embryos with different degrees of axis extension that
1101 correspond to the *dact1* and *dact2* genotypes. Representative lateral images of
1102 embryos at 12 hpf. The yellow line indicates body axis angle measured from the anterior
1103 point of the head, the center of the yolk, to the end of the tail. **B)** Quantification of body
1104 axis angle. Numbers represent the difference in angle relative to the average wildtype
1105 embryo. Asterisk indicates genotypes with angles significantly different from wildtype.
1106 ANOVA $p<0.5$ n= 3-21 embryos. **C)** Representative bud stage wildtype and *dact1/2-/-*
1107 mutant embryos stained for *gsc* (prechordal plate), *pax2a* (midbrain/hindbrain boundary)
1108 and *krox20* (rhombomere 3). Asterisk indicates lack of *krox20* expression in *dact1/2-/-*
1109 mutant. Scale bar = 200 μm **D)** Representative flat mounts of 1-2 ss wildtype and
1110 *dact1/2* mutant embryos stained for *zic1* (telencephalon), *pax2a* and *tbx6* (ventrolateral
1111 mesoderm). **E)** Representative flat mounts of 10 ss wildtype and *dact1/2-/-* mutant
1112 embryos stained for *ctsl1b* (hatching gland), *zic1*, *pax2a*, *krox20*, and *myo1d* (somites).
1113
1114 **Figure 3**. Midface development requires *dact1* and *dact2*. **A)** Representative brightfield
1115 images of wildtype and *dact1/2-/-* compound mutants at 4 dpf. 100 individuals were
1116 analyzed from a *dact1/2*+/- double het cross. Lateral and ventral views show d*act1/2-/-*
1117 compound mutants have a hypoplastic midface, medially displaced eyes, and a
1118 displaced lower jaw. **B)** Representative flat-mount images of Alcian blue stained

1119 ethmoid plate (EP) and visceral cartilage (VC) elements from 4 dpf wildtype and
1120 d*act1/2-/-* compound mutants. d*act1/2-/-* mutants have a rod-shaped EP with no distinct
1121 lateral and medial elements. No obvious differences were found in *dact1/2* mutant VC.
1122 **C)** Representative brightfield image of 4 dpf wildtype and *dact1/2-/-* mutant. Bar
1123 indicates vertebral spine length. Scale bar: 100 μm. **D)** Representative images of Alcian
1124 blue stained *dact1/2-/-*, *wnt11f2-/-,* and *wnt11f2-/-*,*dact1*/2-/- compound mutants.
1125 Embryos resulted from a *dact1+/-,dact2+/-,wnt11f2+/-* in-cross. Lateral and ventral
1126 views show similar craniofacial phenotypes in each mutant. **E)** Representative flat-
1127 mount images of Alcian blue stained EP show a similar phenotype between *dact1/2-/-*,
1128 *wnt11f2-/-,* and *wnt11f2-/-,dact1/2-/-* compound mutants. Scale bar: 200 μm.
1129
1130 **Figure 4.** Anterior neural crest cells of the *dact1/2-/-* mutant migrate to the midline and
1131 populate the dysmorphic ethmoid plate. Lineage tracing of wildtype and *dact1/2-/-*
1132 double mutant zebrafish embryos using Tg(*sox10*:kaede) line. *sox10*:kaede
1133 fluorescence is shown in green and photo-converted kaede is shown in magenta and
1134 highlighted with an arrow. Asterisks indicate that the cell population is absent. **A,B)**19
1135 hpf embryo sagittal views showing photoconversion of anterior-most neural crest
1136 population. At 36 hpf frontal images show the migration of photoconverted neural crest
1137 cells to the frontal prominence in wildtype and *dact1/2-/-* double mutants. At 55 hpf,
1138 frontal images show photoconverted neural crest cells populating the region of the
1139 developing ANC in wildtype and *dact1/2-/-* mutants. At 4.5 dpf ventral images show
1140 photoconverted neural crest cells populating the medial ethmoid plate in wildtype.

1141 Similarly, neural crest cells in *dact1/2-/-* mutants populate the rod-shaped ethmoid plate.
1142 Scale bar:100 μm. Representative images of 3 individual experiments.
1143
1144 **Figure 5.** A nonoverlapping functional role for *dact1*, *dact2,* and *gpc4* and *wls*. **A)**
1145 Representative Alcian blue stained wholemount images of wildtype, *dact1/2-/-* double
1146 mutant, *gpc4-/-* mutant, and *gpc4/dact1/2-/-* triple mutants at 4 dpf. Low magnification
1147 lateral images of embryos showing tail truncation in *dact1/2-/-* mutants, shortened and
1148 kinked tail in *gpc4-/-* mutants, and a combinatorial effect in *gpc4/dact1/2-/-* triple
1149 mutants. Higher magnification lateral images show a shortened midface and displaced
1150 lower jaw in *dact1/2-/-* mutants, a shortened midface in *gpc4-/-* mutant, and a
1151 combinatorial effect in *gpc4/dact1/2-/-* triple mutants. **B)** Representative flat-mount
1152 images of dissected Alcian blue-stained cartilage elements. *dact1/2-/-* mutants have a
1153 narrow rod-shaped ethmoid plate (EP) while *gpc4-/-* mutants have a broad and
1154 shortened EP. *dact1/2/gpc4* triple mutants have a combinatorial effect with a short,
1155 broad rod-shaped EP. In ventral cartilages (VC), *dact1/2-/-* mutants have a relatively
1156 normal morphology while Meckel's cartilage in *gpc4-/-* mutants and *gpc4/dact1/2-/-* triple
1157 mutants is truncated. **C,D)** Same as above except *wls-/-* mutant and *wls/dact1/2-/-* triple
1158 mutant, with similar findings. **E)** Combinatorial genotypes of *dact1*, *dact2,* and *gpc4*.
1159 *dact2-/-* contributed the *dact/gpc4* compound phenotype while *dact1-/-* did not. Scale
1160 bar: 200 μm.
1161
1162 **Figure 6**. Single-cell RNAseq of 4 ss wildtype, *dact1/2-/-* mutant and *gpc4-/-* mutants.
1163 **A)** Summary schematic showing similar phenotypes in *dact1/2-/-* and *gpc4-/-* mutants at

1164 12 hpf and divergent phenotypes at 4 dpf. Single-cell RNAseq was performed during
1165 axis extension to compare and contrast *dact1/2-/-* and *gpc4-/-* transcriptional programs.
1166 UMAP showing cluster identification. **B)** UMAP of cell clusters identified by Single-cell
1167 RNAseq. **C)** Dot plot showing the most differentially expressed genes between clusters.
1168 **D)** UMAP showing *dact1*, *dact2,* and *gpc4* expression in wildtype embryos.
1169
1170 **Figure 7**. Pseudobulk differential expression analysis of single-cell RNAseq data. **A)**
1171 Heatmaps showing the 50 most differentially expressed genes in 3 major cell types;
1172 ectoderm (clusters 4,5,6,7), paraxial mesoderm (clusters 10,11,12), and lateral plate
1173 mesoderm (clusters 15, 16, 17,18) between *dact1/2-/-* mutants and wildtype and *gpc4-/-*
1174 mutants and wildtype. **B)** Venn diagrams showing unique and overlapping DEGs in
1175 *dact1/2-/-* and *gpc4-/-* mutants. **C)** GO analysis of *dact1/2-/-* mutant-specific DEGs in
1176 ectoderm showing enrichment for proteolytic processes.
1177
1178 **Figure 8.** Expression of *capn8* is significantly dysregulated in *dact1/2-/-* mutants. **A)**
1179 Single-cell RNAseq gene expression analysis of *capn8* in wildtype and *dact1/2-/-*
1180 mutants. In wildtype embryos, *capn8* expression is restricted predominantly to the
1181 epidermis whereas *capn8* is widely expressed throughout the embryo in *dact1/2-/-*
1182 mutants, especially in the mesoderm. **B)** Wholemount *in situ* hybridization of *capn8*
1183 expression in wildtype and *dact1/2-/-* mutant embryos at 2 ss. Staining corroborates the
1184 single-cell RNAseq data, with expanded ectopic expression of *capn8* throughout the
1185 embryo**.** Flat mounts are oriented anterior to the left. Scale bar: 100 μm. **C)** Brightfield
1186 images and Alcian blue staining of the ethmoid plate show ectopic expression of *capn8*

1187 mRNA (200 pg) at the 1-cell stage in *dact1+/-*,*dact2+/-* embryos recapitulates the
1188 *dact1/2-/-* compound mutant craniofacial phenotype. The mutant craniofacial phenotype
1189 did not manifest in gfp mRNA (200 pg) injected 1-cell stage *dact1+/-*,*dact2+/-* embryos.
1190 Scale bar: 100 μm **D)** Quantification of mutant and normal craniofacial phenotype in 4
1191 dpf larvae after mRNA injection at the 1-cell stage. Larvae were derived from *dact1/2+/-*
1192 interbreeding. Larvae were uninjected or injected with 200 pg *gfp* control or *capn8*
1193 mRNA. A Fisher exact test showed a significant effect of *capn8* mRNA injecting in the
1194 *dact1/2* double heterozygotes. p= 0.013.
1195
1196 **Supplemental Figures**
1197
1198 **Figure S1.** Daniocell single-cell RNAseq analysis with a display of *dact1*, *dact2*, *gpc4,*
1199 and *wnt11f2* in all cell clusters from 3-120 hpf of development (Farrell, Wang et al.
1200 2018). Cephalic mesoderm (ceph mes), mesenchyme, neural ectoderm, and muscle
1201 clusters are noted.
1202
1203 **Figure S2.** Characterization of CRISPR/Cas9 generated *dact1-/-* and *dact2-/-* mutants.
1204 **A)** Schematic representations of *dact1* and *dact2* exons, positions of guide RNA target
1205 site, introduced premature stop codon (arrow), and sequences of mutations. **B)** DNA
1206 fragment analysis of *dact1+/-* and *dact2+/-* animals showing wildtype (250 and 387 bp
1207 respectively and mutant (228 and 380 bp respectively) **C)** Expression levels of *dact1*
1208 and *dact2* mRNA by RT-qPCR in 12 hpf *dact1-/-* mutants, *dact2-/-* mutants, and
1209 *dact1/2-/-* compound mutants. 8 embryos were pooled for mRNA isolation per sample.

1210 **D)** Injection of *dact1* mRNA, *dact2* mRNA, or a combination of *dact1* and *dact2* mRNA
1211 rescues the rod-shaped ethmoid plate phenotype in *dact1/2-/-* compound mutants.
1212 Representative images of Alcian blue stained *dact1/2-/-* double mutant treated with 300
1213 pg *dact1* mRNA and 300 pg *dact2* mRNA. Arrow highlights normal ethmoid plate (EP).
1214 Visceral cartilage (VC) also appeared normal. **E)** Quantification of the mutant
1215 craniofacial phenotype observed in a *dact1-/-,dact2+/-* breeding in-cross. Without mRNA
1216 injection, the mutant phenotype was observed at approximately (35%) the expected
1217 Mendelian ratio of 25%. Injection with *dact1* mRNA, *dact2* mRNA, or a combination of
1218 *dact1* and *dact2* mRNA decreased the frequency that the mutant craniofacial phenotype
1219 was observed.
1220
1221 **Figure S3.** Loss of *dact1* and *dact2* tends to decrease total body length. **A)**
1222 Representative brightfield images of 4 dpf larvae of compound *dact1* and *dact2* mutant
1223 genotypes. Bar represents *dact1/2+/+* body length measurement. Scale bar: 100 μm. **B)**
1224 Scatter plot of body length measurement of compound *dact1* and *dact2* mutant
1225 genotypes at 4 dpf. ANOVA p=0.06. n=3-4.
1226
1227 **Figure S4.** Cluster abundance across genotype groups. Scatter box plots showing the
1228 frequency of each identified cell cluster between *dact1/2-/-*, *gpc4-/-*, and wildtype
1229 samples.
1230
1231 **Figure S5.** Loss of *gpc4* and loss of *dact1/2* leads to distinct changes in gene
1232 expression profiles but with some overlapping functions. GO analysis of DEGs identified

1233 between *gpc4*-/- and wildtype embryos and *dact1/2*-/- and wildtype embryos found

1234 changes in calcium ion binding and actin interaction in both mutants.

1235

Figure 1

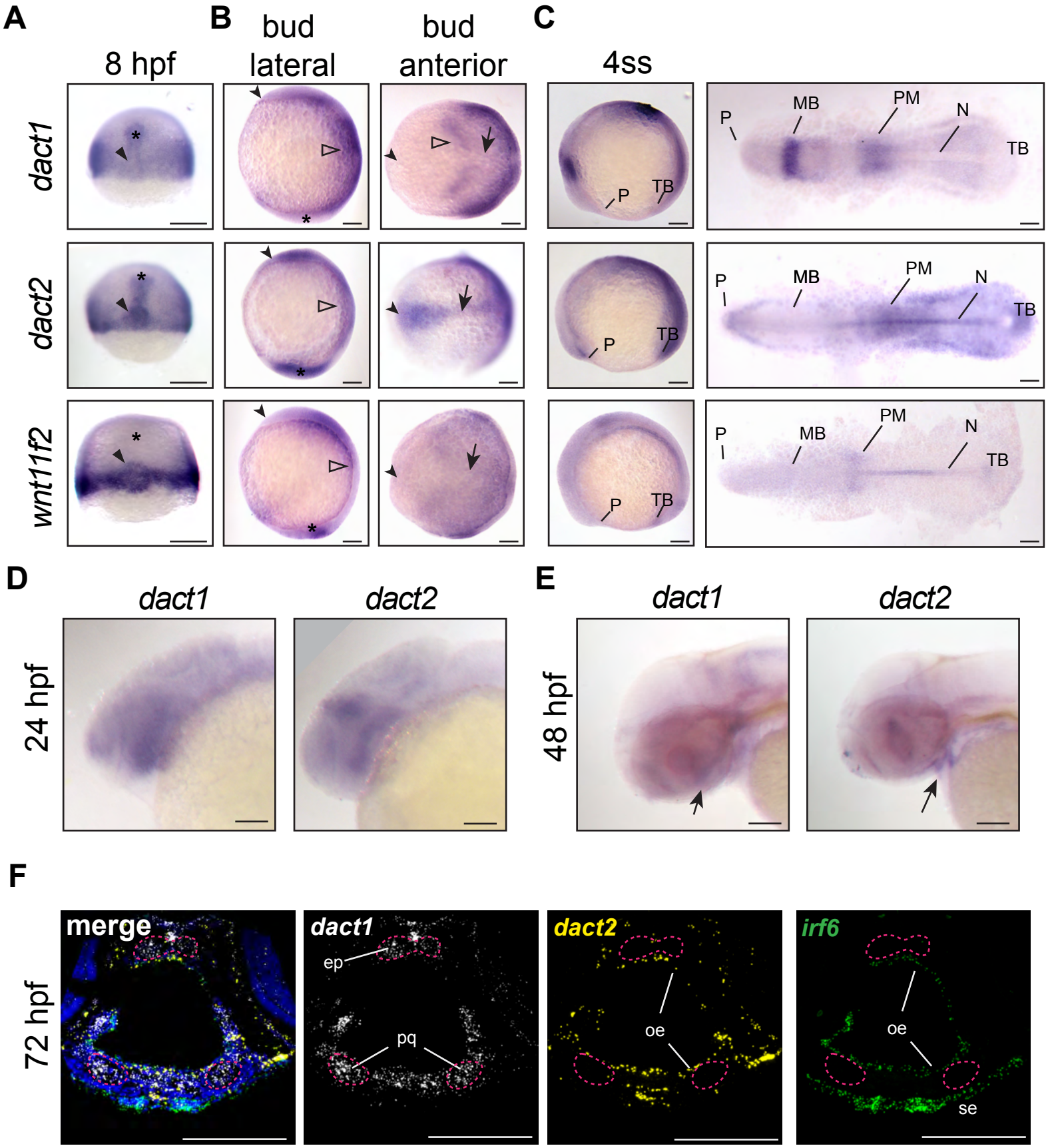
A
B
C
8 hpf
bud lateral
bud anterior
4ss
dact1
dact2
wnt11f2
P
MB
PM
N
TB
D
E
dact1
dact2
24 hpf
48 hpf
F
72 hpf
merge
dact1
dact2
irf6
ep
pq
oe
se

Figure 2

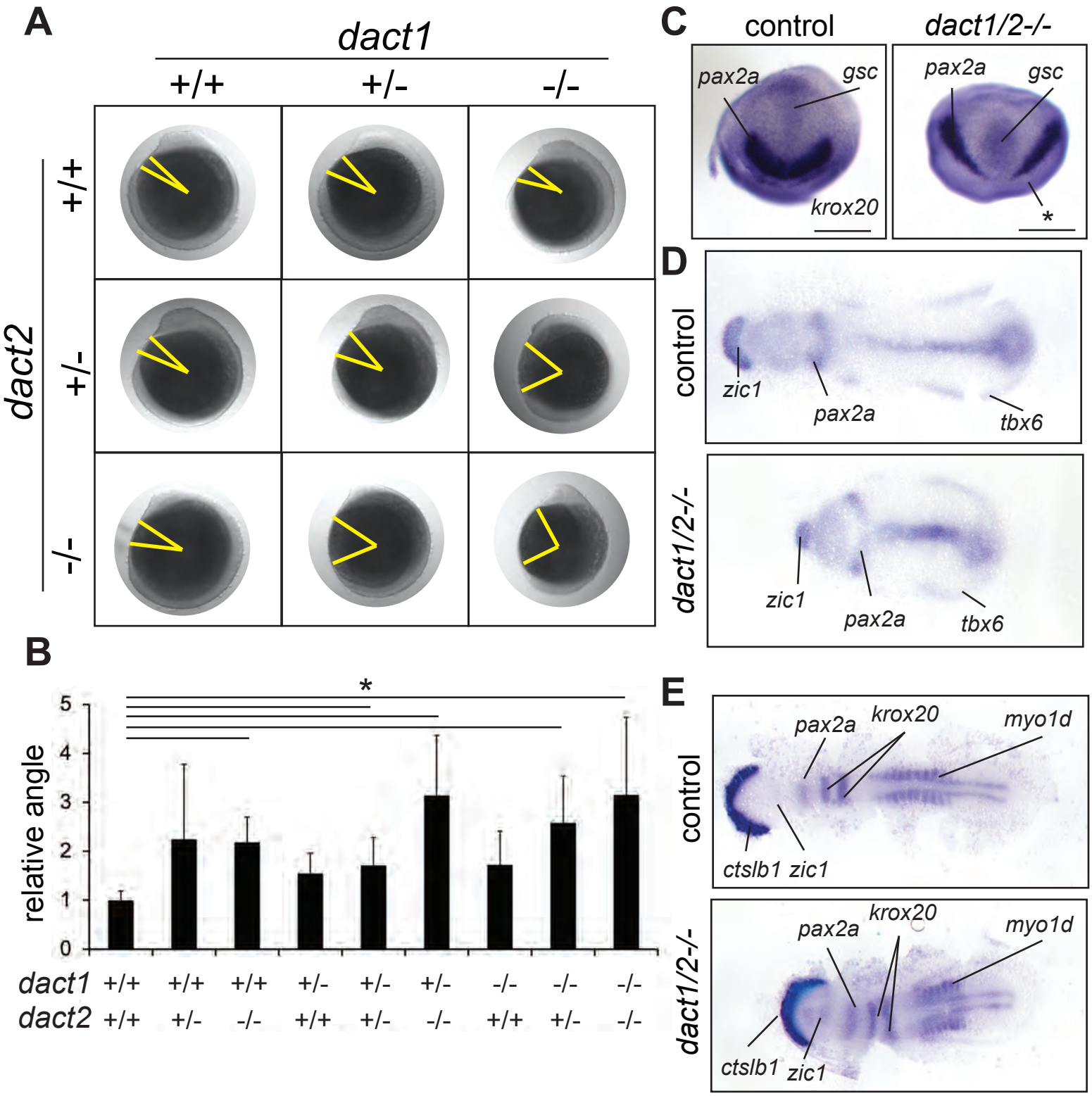
A
dact1
+/+
+/-
-/-
dact2
+/+
+/-
-/-
B
*
relative angle
0
1
2
3
4
5
dact1 +/+ +/+ +/+ +/- +/- +/- -/- -/- -/-
dact2 +/+ +/- -/- +/+ +/- -/- +/+ +/- -/-
C
control
dact1/2-/-
pax2a
gsc
krox20
pax2a
gsc
*
D
control
zic1
pax2a
tbx6
dact1/2-/-
zic1
pax2a
tbx6
E
control
pax2a
krox20
myo1d
ctslb1
zic1
dact1/2-/-
pax2a
krox20
myo1d
ctslb1
zic1

Figure 3

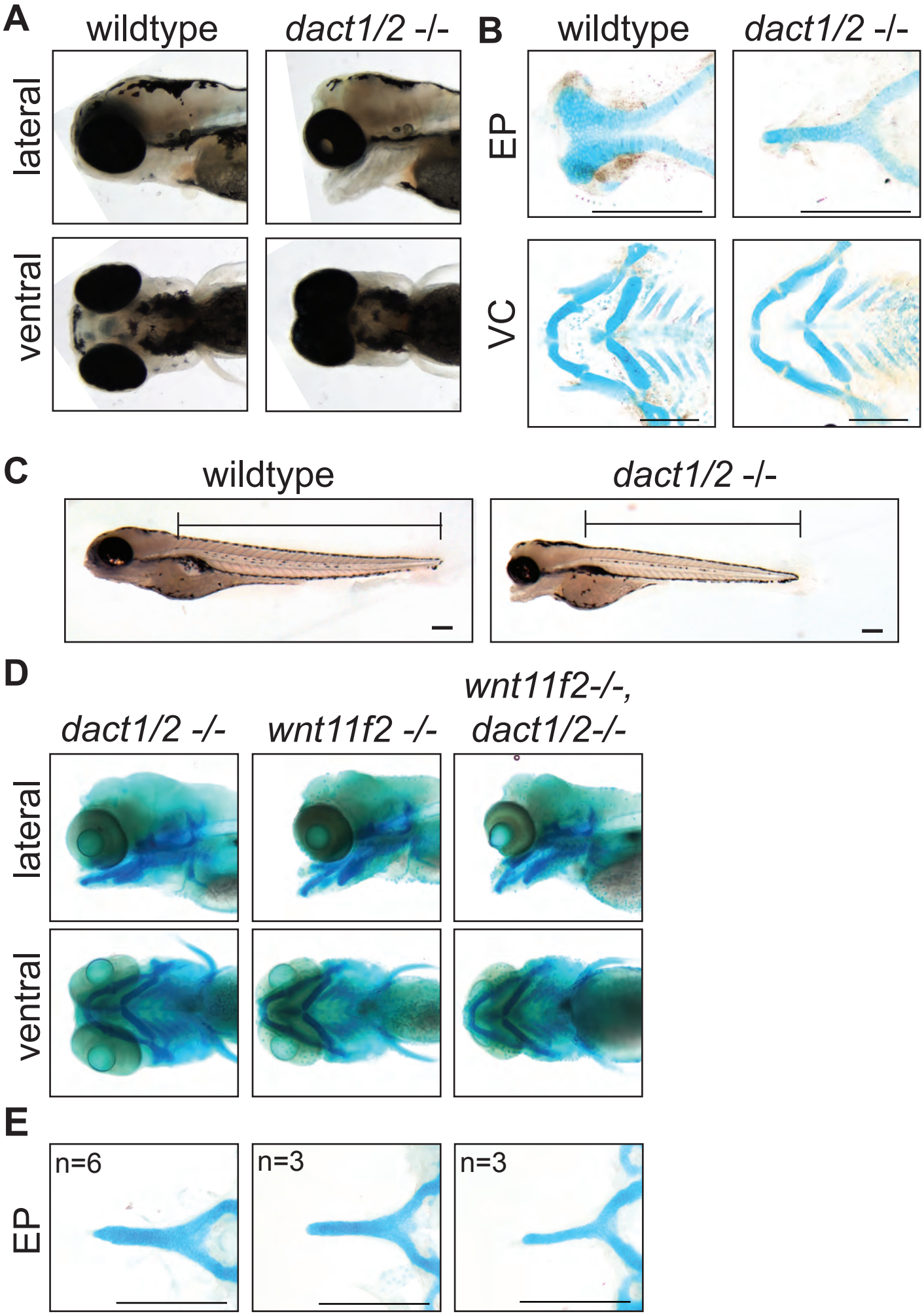
A
wildtype
dact1/2 -/-
lateral
ventral
B
wildtype
dact1/2 -/-
EP
VC
C
wildtype
dact1/2 -/-
D
dact1/2 -/-
wnt11f2 -/-
wnt11f2-/-,
dact1/2-/-
lateral
ventral
E
EP
n=6
n=3
n=3

Figure 4

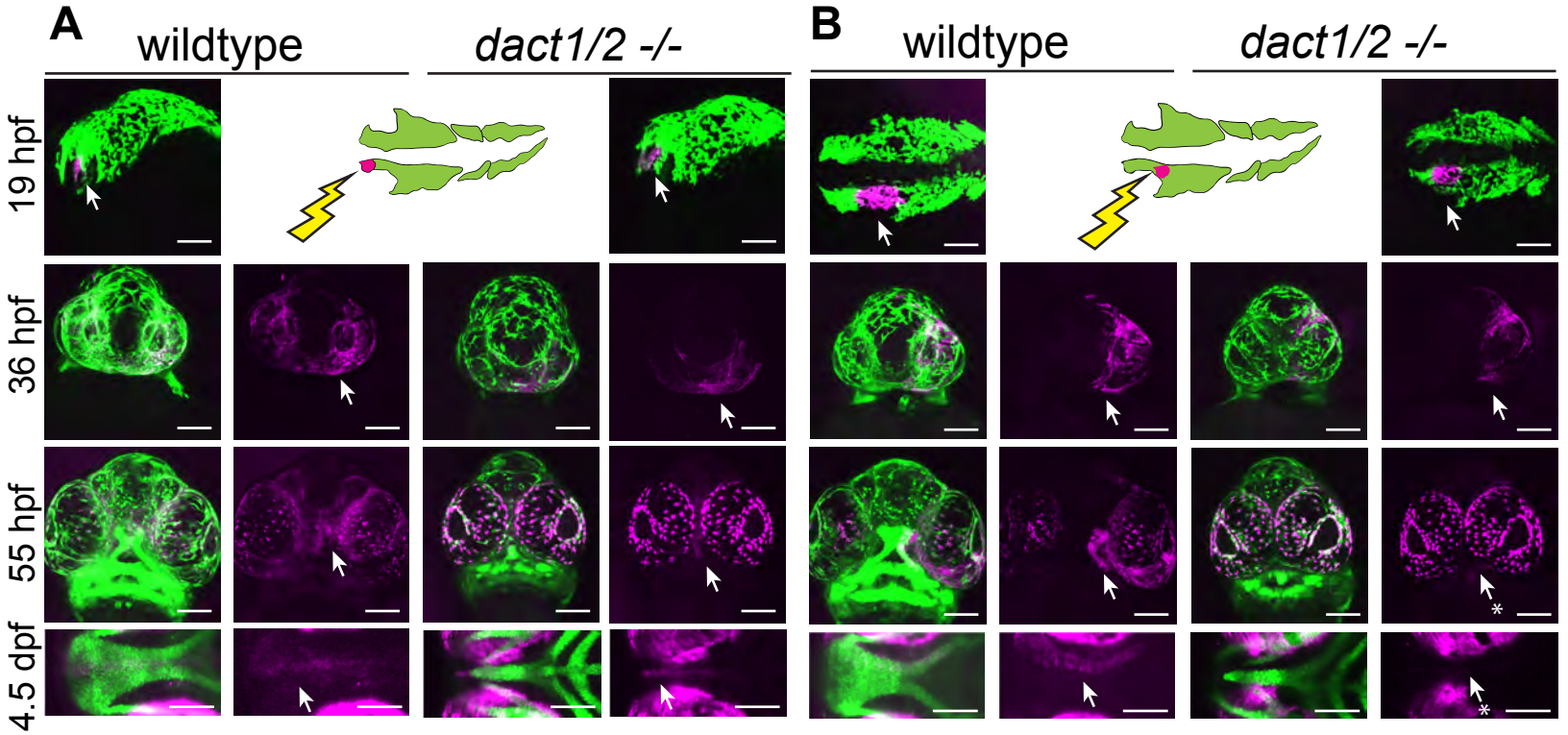
A
wildtype
dact1/2 -/-
B
wildtype
dact1/2 -/-
19 hpf
36 hpf
55 hpf
4.5 dpf

Figure 5

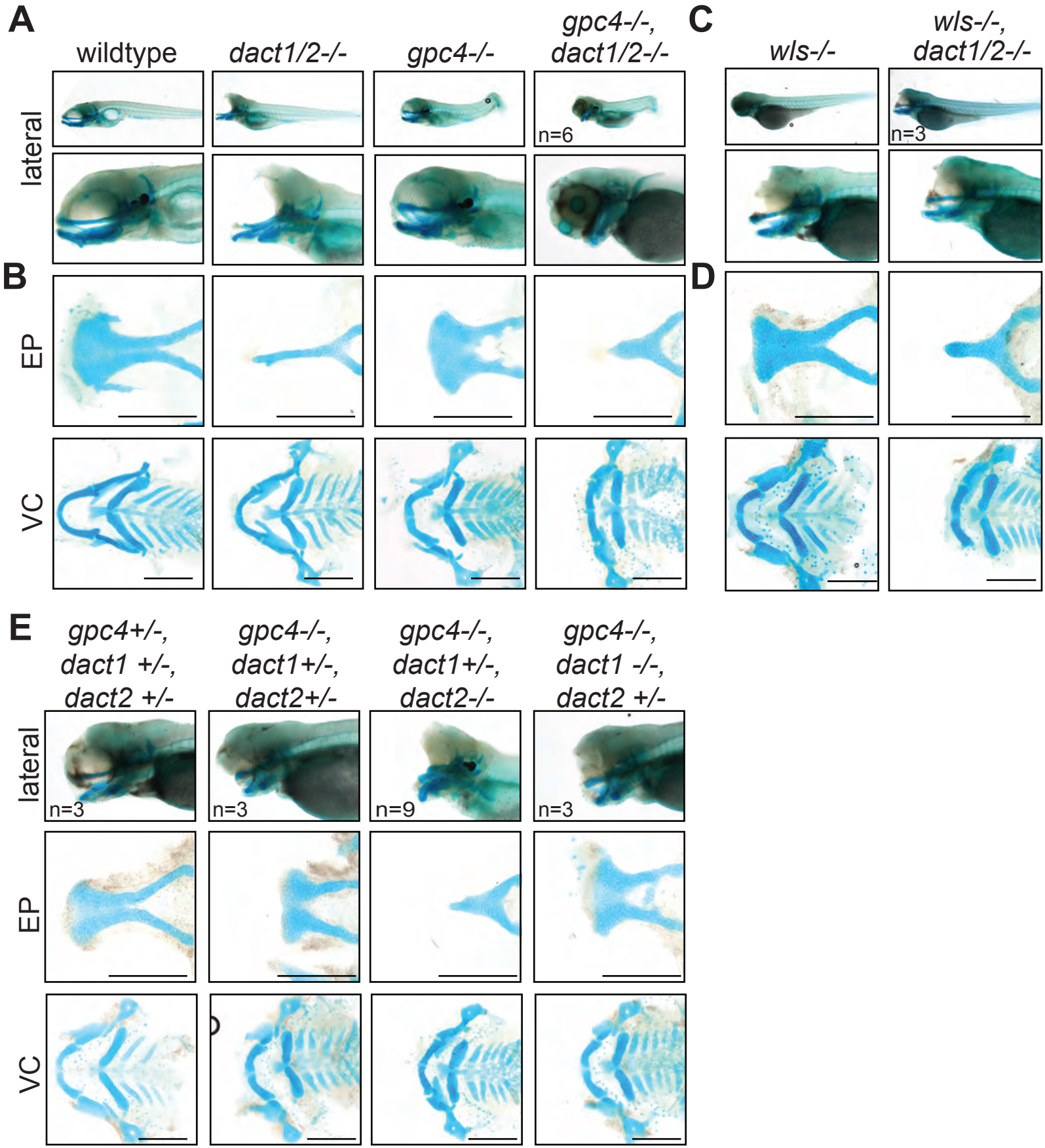
A
wildtype
dact1/2-/-
gpc4-/-
gpc4-/-, dact1/2-/-
lateral
n=6
B
EP
VC
C
wls-/-
wls-/-, dact1/2-/-
n=3
D
E
gpc4+/-, dact1 +/-, dact2 +/-
gpc4-/-, dact1+/-, dact2+/-
gpc4-/-, dact1+/-, dact2-/-
gpc4-/-, dact1 -/-, dact2 +/-
lateral
n=3
n=3
n=9
n=3
EP
VC

Figure 6

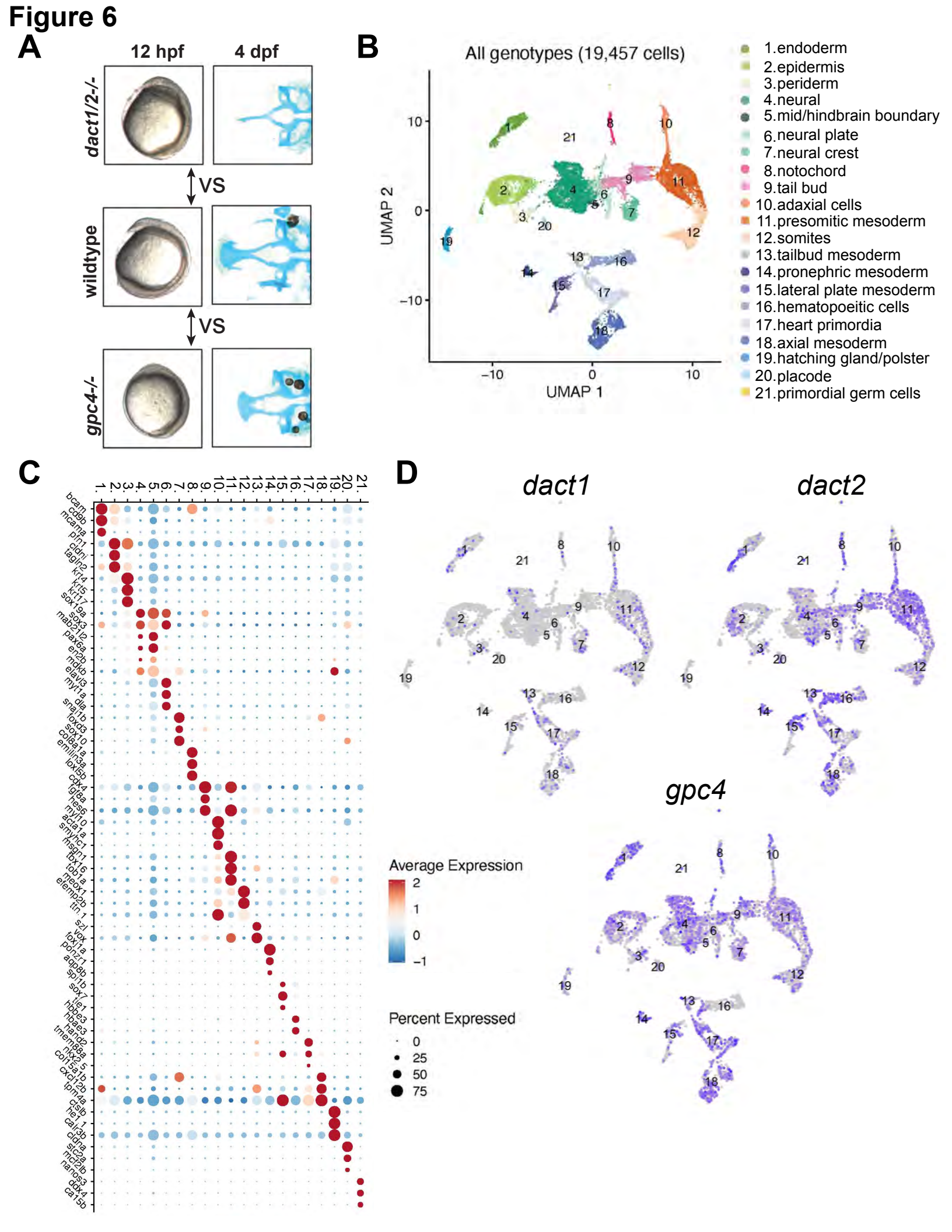
A
12 hpf
4 dpf
dact1/2-/-
VS
wildtype
VS
gpc4-/-
B
All genotypes (19,457 cells)
UMAP 2
UMAP 1
1.endoderm
2.epidermis
3.periderm
4.neural
5.mid/hindbrain boundary
6.neural plate
7.neural crest
8.notochord
9.tail bud
10.adaxial cells
11.presomitic mesoderm
12.somites
13.tailbud mesoderm
14.pronephric mesoderm
15.lateral plate mesoderm
16.hematopoeitic cells
17.heart primordia
18.axial mesoderm
19.hatching gland/polster
20.placode
21.primordial germ cells
C
D
dact1
dact2
gpc4
Average Expression
Percent Expressed

Figure 7

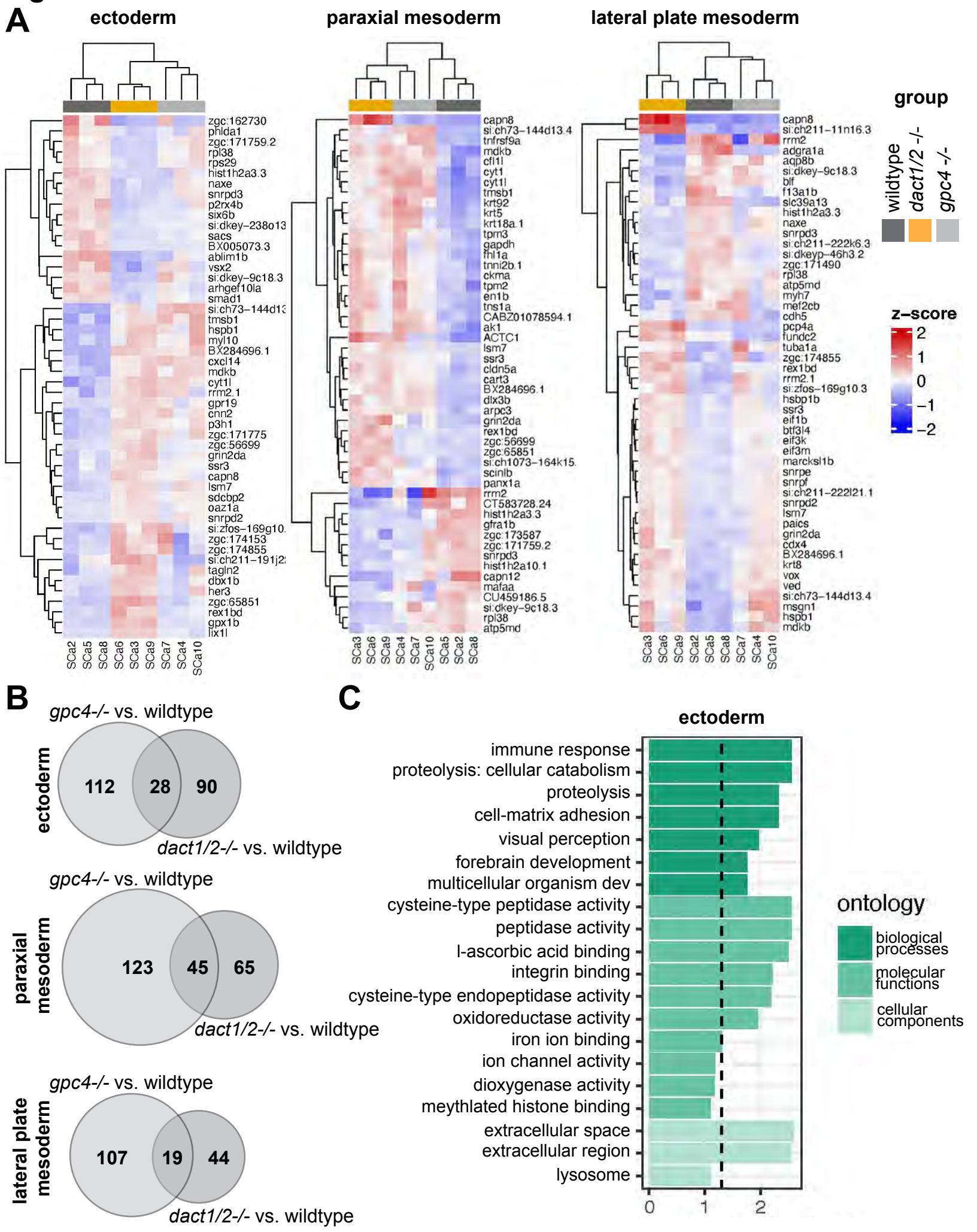
A
ectoderm
paraxial mesoderm
lateral plate mesoderm
group
wildtype
dact1/2 -/-
gpc4 -/-
z-score
2
1
0
−1
−2
B
gpc4-/- vs. wildtype
ectoderm
112
28
90
dact1/2-/- vs. wildtype
gpc4-/- vs. wildtype
paraxial mesoderm
123
45
65
dact1/2-/- vs. wildtype
gpc4-/- vs. wildtype
lateral plate mesoderm
107
19
44
dact1/2-/- vs. wildtype
C
ectoderm
immune response
proteolysis: cellular catabolism
proteolysis
cell-matrix adhesion
visual perception
forebrain development
multicellular organism dev
cysteine-type peptidase activity
peptidase activity
l-ascorbic acid binding
integrin binding
cysteine-type endopeptidase activity
oxidoreductase activity
iron ion binding
ion channel activity
dioxygenase activity
meythlated histone binding
extracellular space
extracellular region
lysosome
0
1
2
ontology
biological processes
molecular functions
cellular components

Figure 8

A

capn8 expression

wildtype

dact1/2-/-

1.floor plate
2.epidermis
3.periderm
4.central nervous system
5.mid/hindbrain boundary
6.spinal cord
7.neural crest
8.notochord
9.tail bud
10.adaxial cells
11.segmental plate
12.paraxial cells/somites
13.tail bud epidermis
14.pronephros
15.vasculogenic/myeloid cells
16.hematopoeitic cells
17.heart field
18.cephalic mesoderm
19.hatching gland/polster
20.otic placode
21.primordial germ cells

B

wildtype

dact1/2-/-

C

dact1+/-, dact2+/-

+ *gfp*

dact1+/-, dact2+/-

+ *capn8*

D

number of individuals

wildtype phenotype

dact1/2-/- phenotype

	uninj	*gfp*	*capn8*	uninj	*gfp*	*capn8*	uninj	*gfp*	*capn8*	uninj	*gfp*	*capn8*	uninj	*gfp*	*capn8*	uninj	*gfp*	*capn8*	uninj	*gfp*	*capn8*	uninj	*gfp*	*capn8*
dact1	+/+			+/+			+/+			+/-			+/-			+/-			-/-			-/-			-/-
dact2	+/+			+/-			-/-			+/+			+/-			-/-			+/+			+/-			-/-

Figure S1

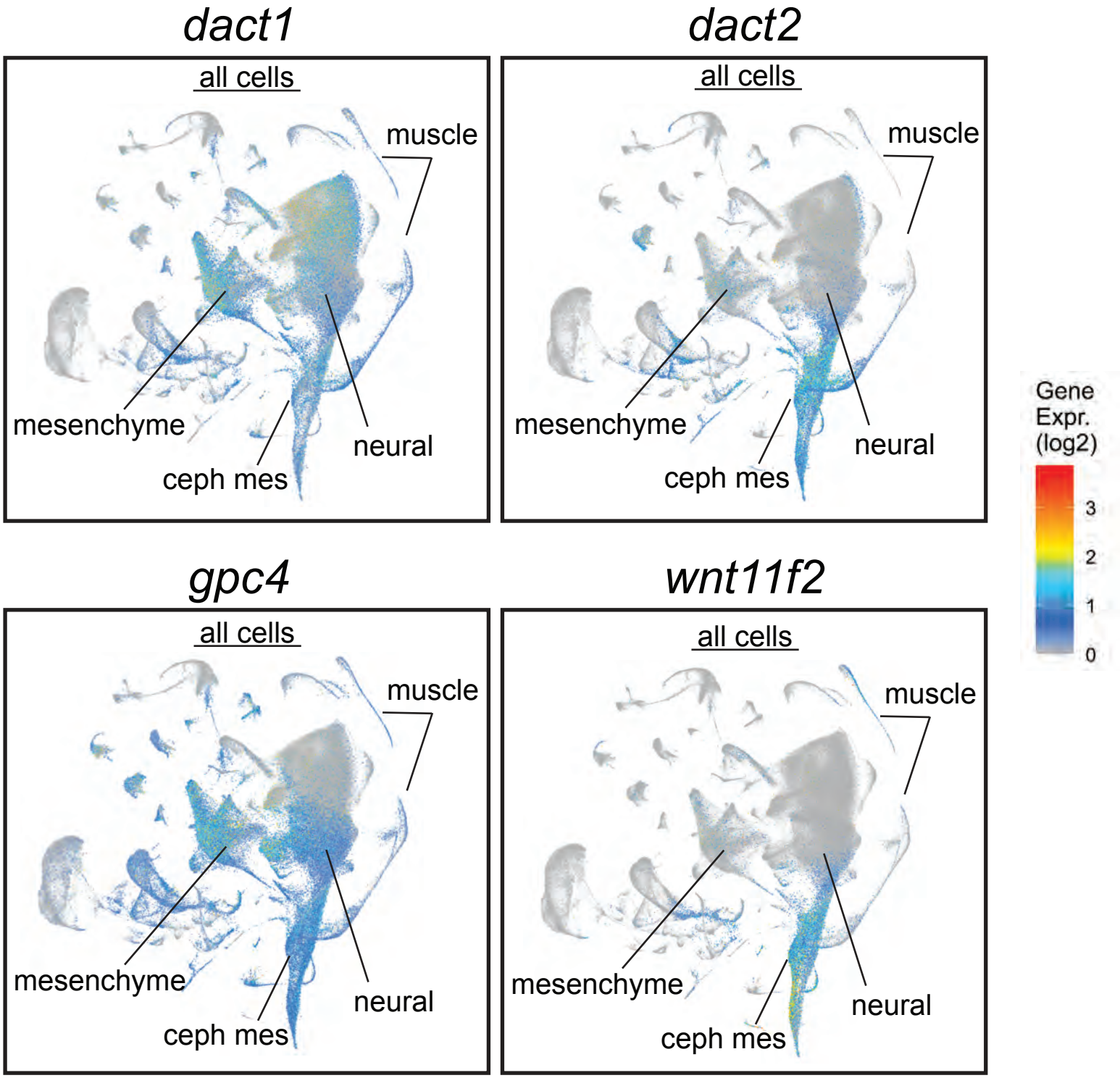
dact1
all cells
muscle
mesenchyme
neural
ceph mes
dact2
all cells
muscle
mesenchyme
neural
ceph mes
gpc4
all cells
muscle
mesenchyme
neural
ceph mes
wnt11f2
all cells
muscle
mesenchyme
neural
ceph mes
Gene Expr. (log2)
3
2
1
0

Figure S2

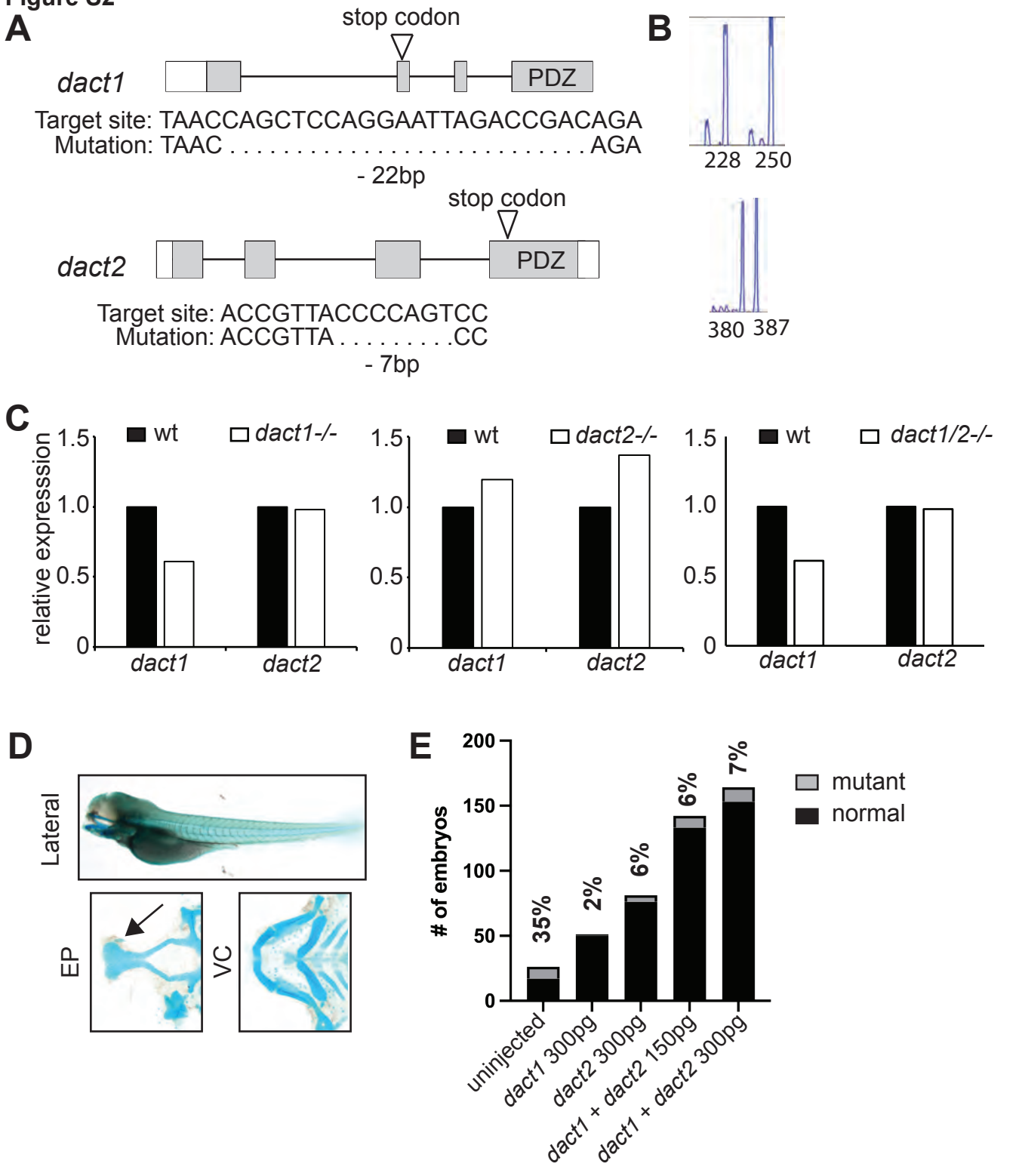
A
stop codon
dact1
PDZ
Target site: TAACCAGCTCCAGGAATTAGACCGACAGA
Mutation: TAAC . . . . . AGA
- 22bp
stop codon
dact2
PDZ
Target site: ACCGTTACCCCAGTCC
Mutation: ACCGTTA CC
- 7bp
B
228 250
380 387
C
relative expresssion
1.5
1.0
0.5
0
wt
dact1-/-
dact1
dact2
wt
dact2-/-
dact1
dact2
wt
dact1/2-/-
dact1
dact2
D
Lateral
EP
VC
E
# of embryos
200
150
100
50
0
35%
2%
6%
6%
7%
mutant
normal
uninjected
dact1 300pg
dact2 300pg
dact1 + dact2 150pg
dact1 + dact2 300pg

Figure S3

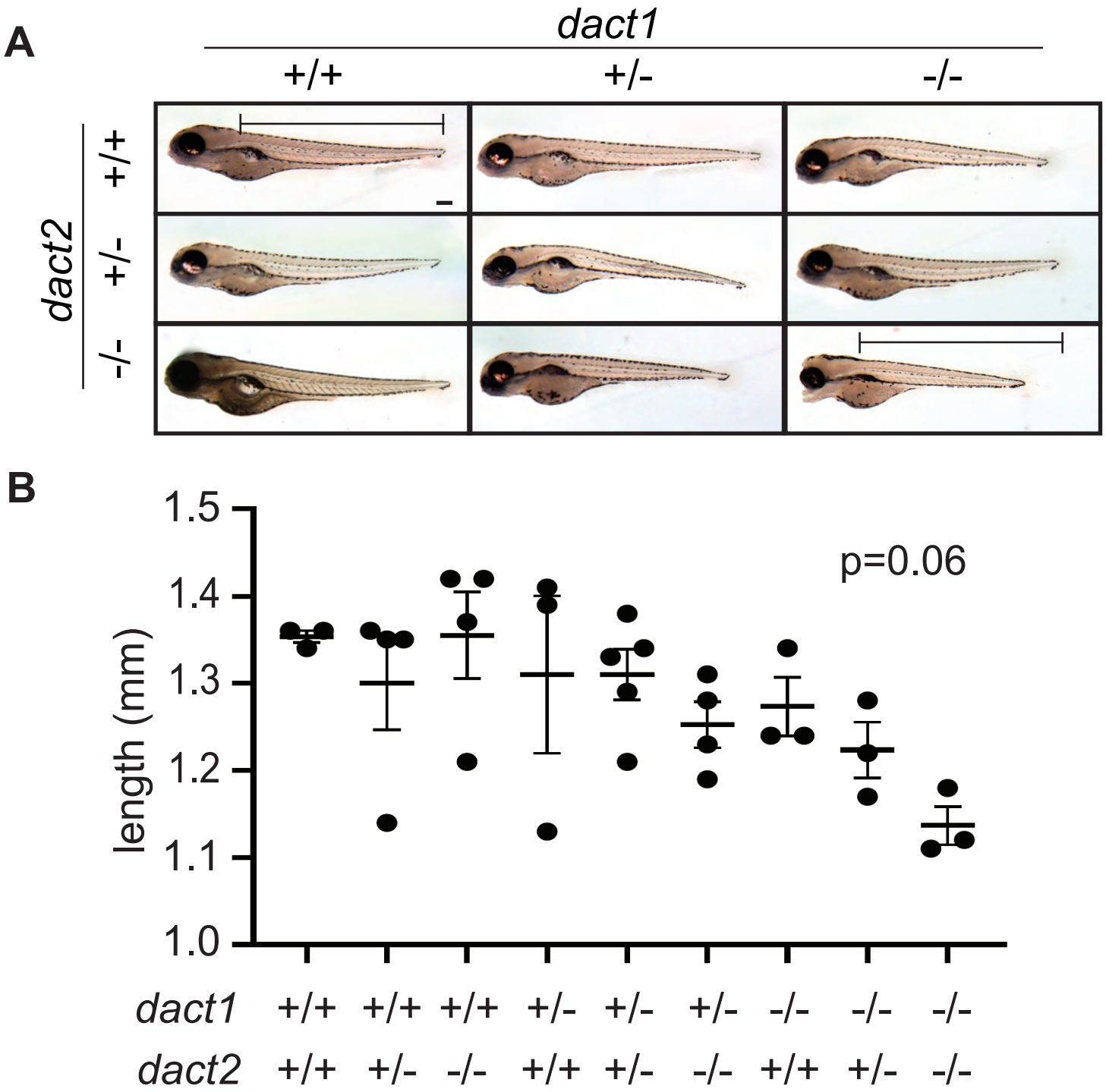

Figure S4

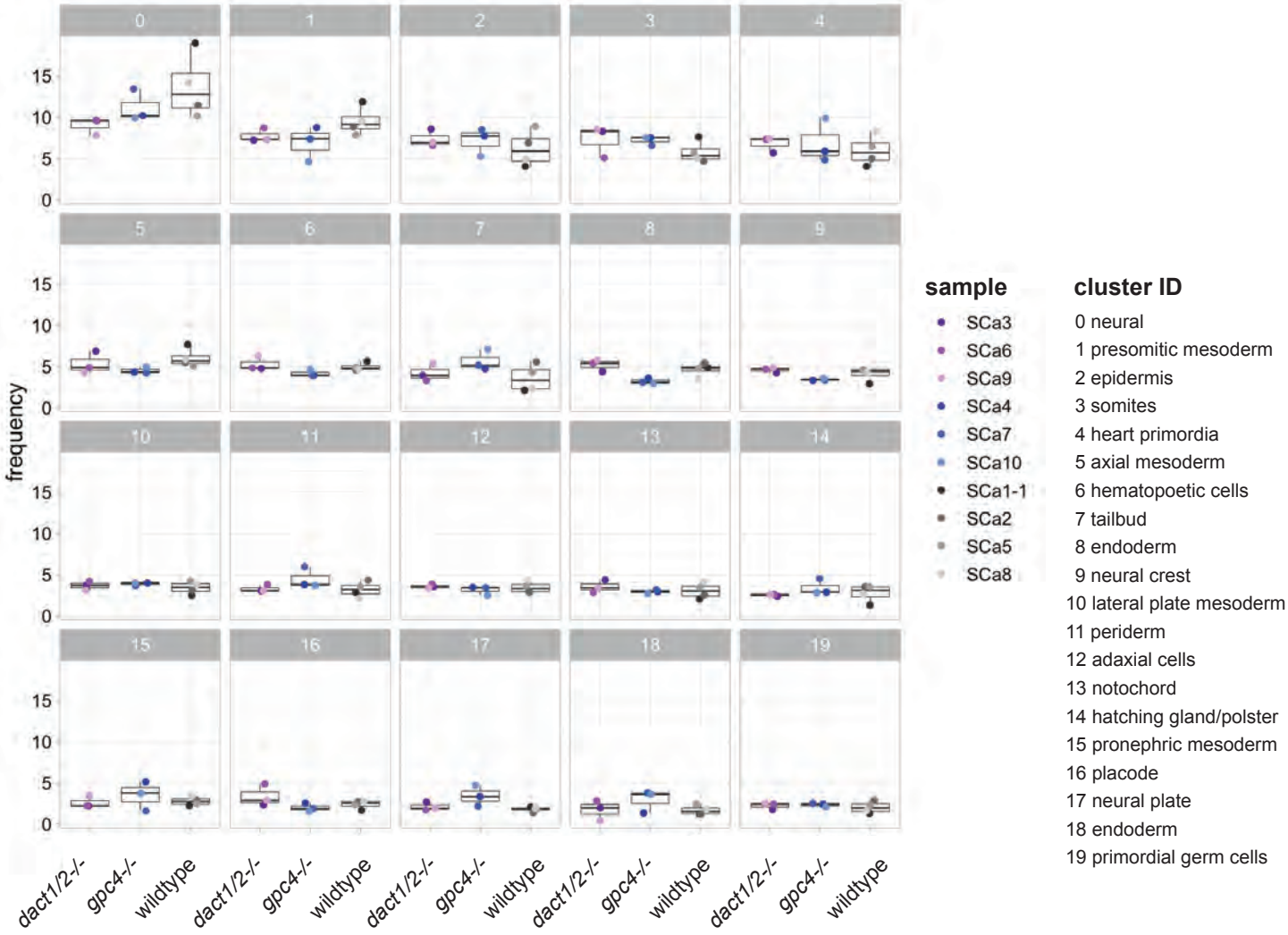
frequency
0
1
2
3
4
5
6
7
8
9
10
11
12
13
14
15
16
17
18
19
dact1/2-/-
gpc4-/-
wildtype
sample
SCa3
SCa6
SCa9
SCa4
SCa7
SCa10
SCa1-1
SCa2
SCa5
SCa8
cluster ID
0 neural
1 presomitic mesoderm
2 epidermis
3 somites
4 heart primordia
5 axial mesoderm
6 hematopoetic cells
7 tailbud
8 endoderm
9 neural crest
10 lateral plate mesoderm
11 periderm
12 adaxial cells
13 notochord
14 hatching gland/polster
15 pronephric mesoderm
16 placode
17 neural plate
18 endoderm
19 primordial germ cells

Figure S5

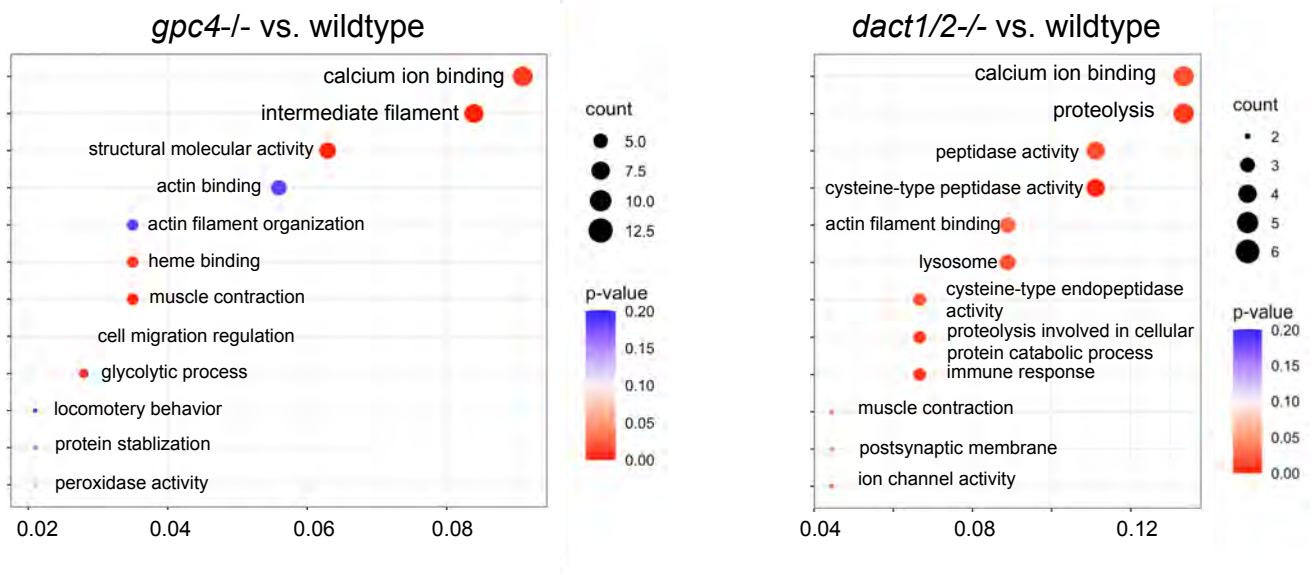
gpc4-/- vs. wildtype
calcium ion binding
intermediate filament
structural molecular activity
actin binding
actin filament organization
heme binding
muscle contraction
cell migration regulation
glycolytic process
locomotery behavior
protein stablization
peroxidase activity
0.02
0.04
0.06
0.08
count
5.0
7.5
10.0
12.5
p-value
0.20
0.15
0.10
0.05
0.00
dact1/2-/- vs. wildtype
calcium ion binding
proteolysis
peptidase activity
cysteine-type peptidase activity
actin filament binding
lysosome
cysteine-type endopeptidase activity
proteolysis involved in cellular protein catabolic process
immune response
muscle contraction
postsynaptic membrane
ion channel activity
0.04
0.08
0.12
count
2
3
4
5
6
p-value
0.20
0.15
0.10
0.05
0.00